# Formation of a mesospheric inversion layer and the subsequent elevated stratopause associated with the major stratospheric sudden warming in 2018/19

**Haruka Okui[1], Kaoru Sato[1], Dai Koshin[1], and Shingo Watanabe[2]**

[1]Department of Earth and Planetary Science, Graduate School of Science, The University of Tokyo, Tokyo, Japan

[2]Japan Agency for Marine–Earth Science and Technology, Yokohama, Japan

Corresponding author: Haruka Okui (okui@eps.s.u-tokyo.ac.jp)

**Key Points:**

- A hindcast of the 2018/19 stratospheric sudden warming was performed using a gravity-wave permitting high-top general circulation model.
- Planetary waves excited by gravity wave forcing cause the formation of a mesospheric inversion layer.
- Both planetary wave and gravity wave forcing contribute to the formation of the subsequent elevated stratopause.

## Abstract

Since 2004, following prolonged stratospheric sudden warming (SSW) events, it has been observed that the stratopause disappeared and reformed at a higher altitude, forming an elevated stratopause (ES). The relative roles of atmospheric waves in the mechanism of ES formation are still not fully understood. We performed a hindcast of the 2018/19 SSW event using a gravity-wave (GW) permitting general circulation model that resolves the mesosphere and lower thermosphere (MLT) and analyzed dynamical phenomena throughout the entire middle atmosphere. An ES formed after the major warming on 1 January 2019. There was a marked temperature maximum in the polar upper mesosphere around 28 December 2018 prior to the disappearance of the descending stratopause associated with the SSW. This temperature structure is referred to as a mesospheric inversion layer (MIL). We show that adiabatic heating from the residual circulation driven by GW forcing (GWF) causes barotropic and/or baroclinic instability before the MIL formation, causing in situ generation of planetary waves (PWs). These PWs propagate into the MLT and exert negative (westward) forcing, which contributes to the MIL formation. Both GWF and PW forcing (PWF) above the recovered eastward jet play crucial roles in ES formation. The altitude of the recovered eastward jet, which regulates GWF and PWF height, is likely affected by the MIL structure. Simple vertical propagation from the lower atmosphere is insufficient to explain the presence of the GWs observed in this event.



## Plain Language Summary

A stratospheric sudden warming (SSW), a rapid and strong warming in the winter polar stratosphere, occurred in January 2019. Following this event, the stratopause disappeared and reformed at a much higher altitude. This phenomenon is called an elevated stratopause (ES), whose formation mechanism is not fully understood. In this study, we conducted hindcast simulations of this SSW event using a high-resolution high-top general circulation model. Prior to the SSW onset, a marked temperature maximum characterized as a mesospheric inversion layer (MIL) appeared in the polar upper mesosphere. We examined the formation mechanisms of the ES and MIL quantitatively and three-dimensionally. The results shows that wave forcing of planetary-scale waves (PWs) caused the ES formation. The MIL is likely caused by both PWs and gravity waves (GWs) which are small-scale waves. In addition, it is inferred that these PWs responsible for the ES and MIL formation were excited from dynamical instability induced by primary GW and PW forcing. These findings indicate that the interplay of PWs and GWs is important for the variation of the stratosphere and mesosphere.



## Index Terms

3334 Middle atmosphere dynamics, 3332 Mesospheric dynamics, 3363 Stratospheric dynamics, 0342 Middle atmosphere: energy deposition, 3389 Tides and planetary waves

**Key words**

Stratospheric sudden warming, elevated stratopause, mesospheric inversion layer, middle atmosphere, gravity waves, planetary waves

## 1 Introduction

Dynamical events called stratospheric sudden warmings (SSWs) greatly alter the thermal and dynamical conditions in the winter stratosphere. They are results of the interaction between upward propagating planetary waves (PWs) and zonal mean fields (Matsuno, 1971). The occurrence of an SSW is indicated by a rapid increase in the temperature and the weakening or reversal of the eastward jet in the winter polar stratosphere. The World Meteorological Organization defines a positive poleward gradient of the zonal mean temperature from 60° latitude to the pole accompanied by a reversal of the zonal-mean zonal wind at 60° latitude at or below 10hPa as a major SSW; a minor SSW only satisfies the first condition. On the basis of the shape of the polar vortex, SSWs can also be classified into displacement and splitting events (e.g., Charlton & Polvani, 2007).

The stratopause descends during SSWs (e.g., Labitzke, 1981). After the onset of the SSWs of 2004, 2006, 2009, 2012, 2013, 2018 and 2019, the lowered stratopause became indistinct and then reformed at an altitude above its climatological height. This phenomenon is called an elevated stratopause (ES) (e.g., Manney et al., 2008, 2009; Siskind et al., 2010). Several previous observational and numerical studies showed that gravity wave (GW) forcing (GWF) induces the formation and descent of the ES (e.g., Tomikawa et al., 2012; Siskind et al., 2007, 2010; Thurairajah et al., 2014). Thurairajah et al. (2014) provided observational evidence of the enhancement of GW activity after SSWs using global high-latitude temperature measurements from the Solar Occultation for Ice Experiment (SOFIE). Using a GW-permitting general circulation model (GCM) of the KANTO project (Watanabe et al., 2008), Tomikawa et al. (2012) analyzed a simulated major SSW event. They showed that positive PW forcing (PWF) leads to the quick recovery of the polar eastward jet after the major SSW (Orsolini et al., 2017), and negative GWF above the recovered jet contributes to the formation of the ES.

The crucial role of PWs in the initial phase of ES formation has also been suggested (e.g., Limpasuvan et al., 2012, 2016; Chandran et al., 2011, 2013). Limpasuvan et al. (2016) conducted a composite analysis of 13 SSW-ES events identified in the runs of the Whole Atmosphere Community Climate Model, Version 4 with specified dynamics (SD-WACCM) for 1990–2013. They showed that downward flow induced by negative PWF in the polar mesosphere and lower thermosphere (MLT) is responsible for ES formation. Several observational studies have pointed out that the amplitudes of PWs with zonal wavenumber $s$= 1–2 increase in the MLT when an ES event occurs (e.g., Stray et al., 2015). However, it has

also been indicated that PWF in the MLT is not necessarily strong during ES formation. Chandran et al. (2013) showed that in a few events in model simulations, the entire process of ES formation appears to be driven by GWF despite the climatological importance of PWF. The relative contributions of GWs and PWs to ES formation remain to be elucidated.

The ES phenomenon, which is accompanied by downwelling in the MLT, strongly influences downward material transport and thus the coupling between the MLT and the stratosphere (e.g., Randall et al., 2009). For example, NOx (=NO+$NO_2$) produced by energetic particle precipitation (EPP) in the MLT is transported into the stratosphere, especially during ES events that occur in early winter. In the region under the influence of the polar night, NOx is long-lived and causes ozone depletion in the stratosphere (e.g., Holt et al., 2013; Randall et al., 2009). This effect, referred to as the EPP indirect effect, is very important in chemistry–climate models because it affects the dynamics of the stratosphere (e.g., Siskind et al., 2015). Smith et al. (2018) also pointed out that the enhanced downward flow associated with ES events results in a downward shift in the maximum altitude of ozone concentrations.

However, most high-top models tend to underestimate downward material transport in the MLT during ES events (e.g., Randall et al., 2015; Orsolini et al., 2017). In addition, ES height is generally lower in the model than in observational data. These model biases are the results of the underestimation (overestimation) of downward motion in the upper (lower) mesosphere (e.g., Funke et al., 2017). Meraner et al. (2016) showed that the intensity of the parameterized nonorographic GW sources affects the height of GWF in the MLT. The modulation of the height of GWF can affect the amount of downward material transport. They reported that weaker GW sources in the parameterization yield a better agreement of simulations with observations.

To elucidate the relative importance of PWs and GWs in dynamical variation in the middle atmosphere associated with an SSW, the in-situ generation of waves should be taken into consideration. Several studies showed that strong PW breaking causes the barotropic (BT) and/or baroclinic (BC) instability, which excites PWs (e.g., Baldwin & Holton, 1988; Hitchman & Huesmann, 2007; Greer et al., 2013). Smith (1996, 2003) and Lieberman et al. (2013) suggested that momentum deposition by the GWs that have been filtered by planetary-scale wind structures in the stratosphere lead to in situ generation of PWs in the middle and upper mesosphere. On the basis of a case study of a boreal winter using the KANTO model, Sato and Nomoto (2015) suggested the importance of the interplay of GWs and PWs in the middle atmosphere. They provided evidence of in-situ PW generation due to the BT/BC instability resulting from the generation of a potential vorticity (PV) maximum attributed to GWF. Positive and negative PWFs associated with the PW generation act to eliminate this PV maximum. Using the KANTO model, Watanabe et al. (2009) showed that in the Antarctic winter mesosphere eastward 4-day waves are generated by the BT/BC instability which

develops in the large-scale mean flow strongly distorted by GWF. Sato et al. (2018) and Yasui et al. (2018) showed that the BT/BC instability and shear instability caused by GWs originating from the lower atmosphere generate PWs and GWs in the mesosphere, respectively.

Most high-top GCMs include GW parameterizations. In general, GW parameterization schemes assume that GWs originate only from the lower atmosphere. In-situ generation of GWs in the middle atmosphere is ignored in these parameterizations. Recently, Vadas and Becker (2018) suggested that momentum deposition associated with the breaking of orographic GWs generates secondary GWs in the stratosphere and lower mesosphere in the southern polar region in winter. In addition, most standard GW parameterizations also assume that GWs propagate only vertically. However, using the KANTO model, Sato et al. (2009; 2012) showed evidence of lateral propagation of GWs and provided theoretical explanations of the mechanisms involved. Conducting ray-tracing simulations, Yamashita et al. (2013) also suggested that high GW activity in the MLT during ES events observed by the Sounding of the Atmosphere using Broadband Emission Radiometry (SABER) on the Thermosphere, Ionosphere, Mesosphere Energetics Dynamics (TIMED) satellite is caused by poleward propagating GWs (Thurairajah et al., 2020). To understand the middle atmosphere dynamics in which behavior of the GWs is one of the key processes, state-of-the-art GW-permitting GCMs provide an effective approach.

In this study, we used a high-top and GW-permitting GCM to examine the SSW-ES event that occurred in January 2019. We focus on the relative roles of GWs and PWs to elucidate the mechanism of temperature variations in the middle atmosphere including the ES. Since GWs are explicitly resolved in the model, the in-situ generation and lateral propagation of GWs are also simulated. The 2018/19 SSW event is classified as a mixture of displacement-type (s= 1) and split-type (s=2) SSW (Rao et al. 2019). Three-dimensional analysis methods are applied wherever possible because zonal asymmetry is pronounced especially in the ES structures associated with displacement-type SSWs (Chandran et al., 2014; France & Harvey, 2013). The methods of analysis and details of the model used in this study are described in section 2. In section 3, the observed temperature variations associated with the SSW and their possible mechanisms are discussed. Section 4 focuses on the sources of PWs playing important roles in these mechanisms. Characteristics of both PWs and GWs observed in the middle atmosphere are shown in section 5. Summary and concluding remarks are given in section 6.

## 2 Methods and model description

In this study, we simulated the 2018/19 SSW event using the Japanese Atmospheric General circulation model for Upper Atmosphere Research (JAGUAR) (Watanabe & Miyahara, 2009). The model has 340 vertical layers from the surface to a geopotential height of approximately 150 km with a log-pressure height interval of 300 m throughout the middle

atmosphere and a horizontal, triangularly truncated spectral resolution of T639 that has a minimum resolvable horizontal wavelength of ~60 km (a latitudinal interval of 0.1875°). No parameterization for subgrid-scale GWs was used in this study.

It is considered that this model can resolve major part of GWs which can be inherently distributed over a wide horizontal wavelength range. Using continuous mesospheric wind observation data over 50 days from a mesosphere-stratosphere-troposphere radar called the PANSY radar at Syowa Station (69.0° S, 39.6° E), where PANSY stands for Program of the Antarctic Syowa MST/IS radar, Sato et al. (2017) showed that GW momentum fluxes are mainly associated with waves having long periods of several hours to a day at the southern high latitudes in summer. Using observational data from the PANSY radar, Shibuya et al. (2017) and Shibuya and Sato (2019) showed the GWs having such long periods are dominant also in the winter mesosphere and their horizontal wavelengths are greater than 1,000 km and vertical wavelengths of about 14 km. Ern et al. (2018) analyzed the satellite observation data and showed that dominant GWs in the middle atmosphere on average have horizontal wavelengths greater than 1,000 km and vertical wavelengths in excess of 10 km, although the observational filter problem remains. In the lower stratosphere, Sato (1994) showed that dominant inertia-GWs have horizontal wavelengths of 300–400 km based on three-year observations by the MU radar (35° N, 136° E) in Japan. These dominant horizontal and vertical wavelengths are resolvable by the model used in the present study.

The KANTO model, which is a prototype of JAGUAR, is T213L256 GCM whose minimum resolvable horizontal wavelength is 180 km. Watanabe et al. (2008) showed that GW amplitudes simulated by the KANTO model were consistent with the observations in the lower stratosphere by the MU radar (Sato, 1994) and those obtained by a radiosonde observation campaign in the middle Pacific over a wide latitudinal range from 28° N to 48° S (Sato et al., 2003). In addition, the model reproduced GWs having characteristic phase structure with horizontal wavelengths of ~300 km in the middle stratosphere over the region near Patagonia and Antarctic Peninsula which are similar to the satellite (AIRS) observations with high horizontal resolutions (Sato et al., 2012). These facts mean that dominant GWs simulated by the KANTO model are realistic in terms of the wave structure and amplitude. In addition, Watanabe et al. (2008) demonstrated that the KANTO model could generally reproduce realistic zonal mean zonal wind in the middle and upper mesosphere in which GWF plays a critically important role. This fact suggests that the momentum transport and its deposition by all resolved GWs in the middle atmosphere in the model also quantitatively mimic the real atmosphere, and hence the simulation data can be used as a surrogate of the real atmosphere. The JAGUAR model was developed based on the KANTO model. Thus, it is considered that the model used in this study could also reproduce a major part of GWs in the middle atmosphere, but over a wider horizontal wavelength range than the KANTO model.

Koshin et al. (2020) recently developed a four-dimensional local ensemble transform Kalman filter (4D-LETKF) assimilation system in a medium-resolution (T42L124, a latitudinal interval of 2.8125°) version of the JAGUAR, which called Japanese Atmospheric GCM for Upper Atmosphere Research-Data Assimilation System; JAGUAR-DAS. They assimilated the PrepBUFR observational dataset provided by the National Centers for Environmental Prediction (NCEP), including temperature, wind, humidity, and surface pressure from radiosondes, aircrafts, wind profilers, and satellites, and satellite temperature data from the Aura Microwave Limb Sounder (MLS). Koshin et al. (2021) improved the quality of the analysis data by introducing a filter called incremental analysis updates (Bloom et al., 1996) and assimilating the temperature data from SABER and brightness temperature data from Special Sensor Microwave Imager/Sounder (SSMIS). Using the analysis data from December 2018 to January 2019 produced by the JAGUAR-DAS as initial values for the high-resolution JAGUAR, a hindcast of the 2018/19 SSW event was carried out here. The time period of simulation is from 5 December 2018 to 17 January 2019. This time period was divided into consecutive periods of 4 days. An independent model run was performed for each 4-day period. Each model run consists of 3-day spectral nudging and 4-day free run. We analyzed the output data from the 4-day free runs.

The transformed Eulerian mean (TEM) primitive equations were used for diagnosing wave forcing and residual mean circulation (e.g., Andrews & McIntyre, 1976). In the TEM system, the Eliassen–Palm (EP) flux represents the direction of wave activity flux and its divergence [EPFD= $(\rho_0 a \cos\varphi)^{-1}\boldsymbol{\nabla}\cdot\mathbf{F}$, where $\rho_0$ is reference density, $\varphi$ is the latitude, $a$ is the earth's radius and $\mathbf{F}$ is the EP flux] represents wave forcing. Positive (negative) EPFD represents eastward (westward) momentum deposition by waves. In the present study, 'positive (negative)' wave forcing means eastward (westward) momentum deposition.

In addition, to visualize the longitudinal structure of the residual mean circulation, we calculated three-dimensional residual mean vertical flow using the formula derived by Kinoshita et al. (2019):

$$\overline{w}^* = \overline{w} + \left(\frac{\overline{u_\mathrm{g}\theta}}{\theta_{0z}}\right)_x + \left(\frac{\overline{v_\mathrm{g}\theta}}{\theta_{0z}}\right)_y \qquad (1)$$

where overbar represents the time mean, and $u_\mathrm{g}$ and $v_\mathrm{g}$ are geostrophic zonal and meridional flows, respectively; the suffixes $x$, $y$ and $z$ denote the respective partial derivatives in the zonal, meridional and vertical directions; $\theta$ and $\theta_0$ are the potential temperature and reference potential temperature, which is defined as $\theta_0 = (\mathrm{g}H/R)e^{\kappa z/H}$; g represents the gravitational acceleration; $H$ is scale height (= 7 km); $R$ is the gas constant of dry air; $\kappa$ is a dimensionless value and is defined as $R/c_p$, where $c_p$ denotes specific heat at constant pressure. Equation (1) is the deformed form of the original equation of $\overline{w}^*$ in Kinoshita et al. (2019), using $[A]_x = 0$ and $[v_\mathrm{g}] = 0$, where $[A]$ denotes the zonal mean of $A$. This vertical

240 flow contains the Stokes drift associated with transient and stationary waves. Moreover,
241 adiabatic vertical motions along the undulated isentropic surfaces associated with the stationary
242 waves are excluded. Thus, equation (1) represents the diabatic flow crossing the isentropic
243 surfaces. In this study, we set the period of the time mean to four days.

244 To analyze three-dimensional wave propagation, we also used a three-dimensional
245 wave activity flux of Kinoshita and Sato (2013), namely 3D-flux-W. The components of 3D-
246 flux-W that are associated with the flux of zonal momentum are as follows:

$$\mathbf{F}_{W1} = \rho_0 \begin{pmatrix} \frac{1}{2}\left(\overline{u'^2} - \overline{v'^2} + \frac{\overline{\Phi_z'^2}}{N^2}\right) \\ \overline{u'v'} \\ \overline{u'w'} - f\frac{\overline{v'\Phi_z'}}{N^2} \end{pmatrix} \tag{2}$$

247 where $N^2$ is the static stability (the square of the Brunt-Väisälä frequency) and $\Phi$ is
248 geopotential. The prime means wave component. This formula was originally derived for
249 transient waves, but they hold for stationary waves if the wave component is extracted properly
250 and an appropriate average is made (Sato et al., 2013). To analyze the wave activity fluxes
251 associated with both transient and stationary PWs, we examined components having zonal
252 wavenumbers $s$= 1–3 as the perturbation field and applied an extended Hilbert transform
253 proposed by Sato et al. (2013) to eliminate phase dependency of waves instead of time
254 averaging. Kinoshita and Sato (2013) showed that the 3D-flux-W approximately parallel to the
255 group velocity of Rossby waves. In the figures that follow, each component of $\mathbf{F}_{W1}$ is shown
256 with the sign reversed to match the direction of the group velocity of Rossby waves.

257 For the analysis of the dynamical stability of mean flow, we used the modified potential
258 vorticity (MPV) defined by Lait (1994) as the Ertel's potential vorticity weighted by $\theta^{-9/2}$. In
259 this paper, MPV is denoted by $P_M$. It roughly represents the product of absolute vorticity and
260 $N^2$ including perturbations (e.g., Sato & Nomoto, 2015).

261

262 **3 Overview of the 2018/19 SSW event**

263 3.1 Time variations of the zonal mean fields

264 The onset of the major warming occurred on 1 January 2019. Figure 1 shows the time–
265 height sections of zonal mean zonal wind $[u]$ and zonal mean temperature $[T]$ from the
266 model results (Figs. 1a and 1c), the Modern-Era Retrospective analysis for Research and
267 Applications, Version 2 (MERRA-2, Figs. 1b and 1d) and satellite temperature from the Aura
268 MLS and TIMED SABER. Temperature from the MLS has been bias-corrected with TIMED
269 SABER data (Koshin et al., 2020). The stratospheric $[u]$ and $[T]$ in the JAGUAR results
270 agree well with those in the MERRA-2.

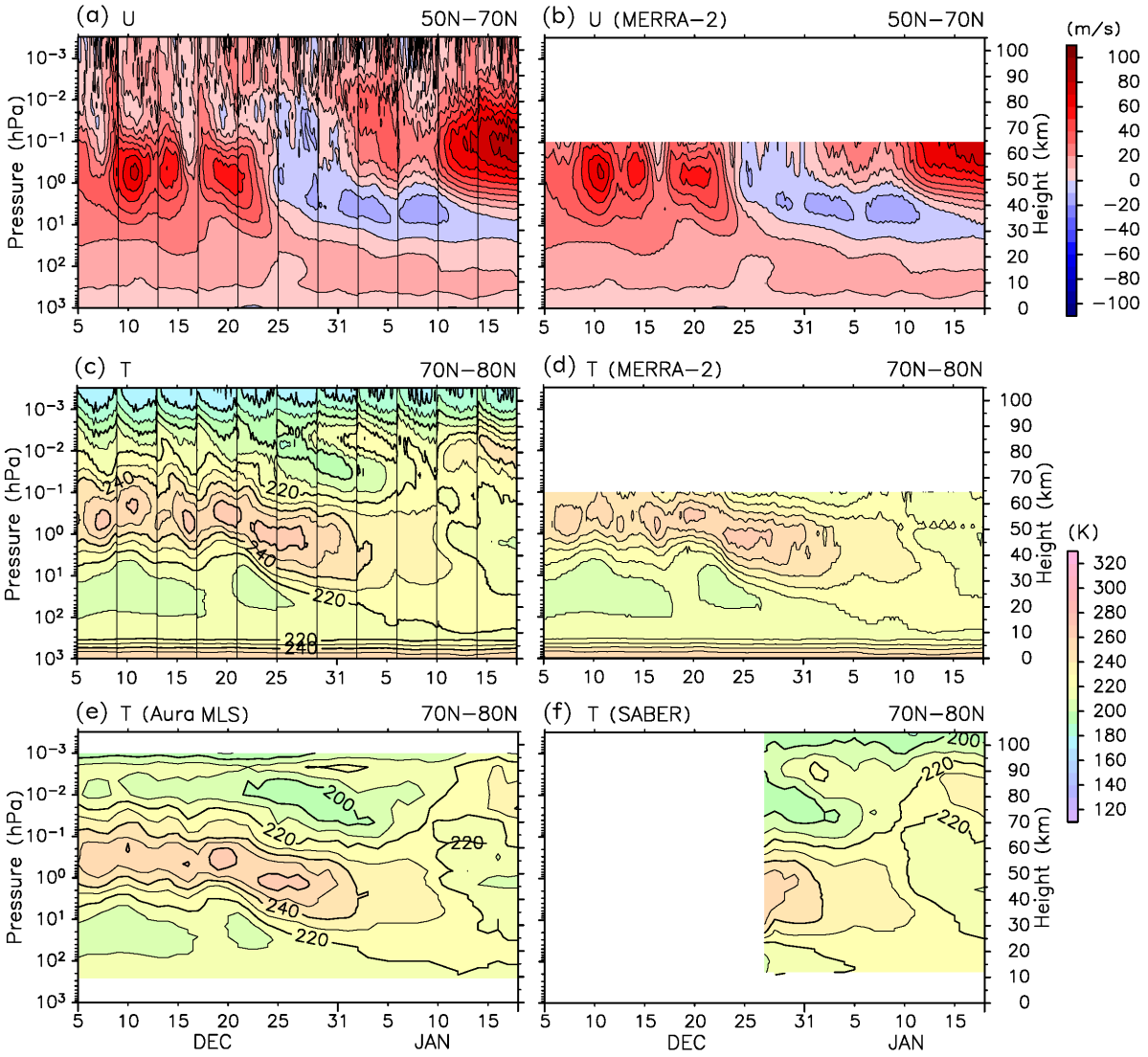


**Figure 1**. Time–height sections of $[u]$ averaged over 70° N–80° N from (a) the JAGUAR-T639L340 simulation and (b) MERRA-2 reanalysis data, and $[T]$ averaged over 50° N–70° N from (c) the JAGUAR-T639L340 simulation (d) MERRA-2, (e) Aura MLS and (f) SABER. Vertical lines in (a) and (c) represent the boundaries of the model runs.

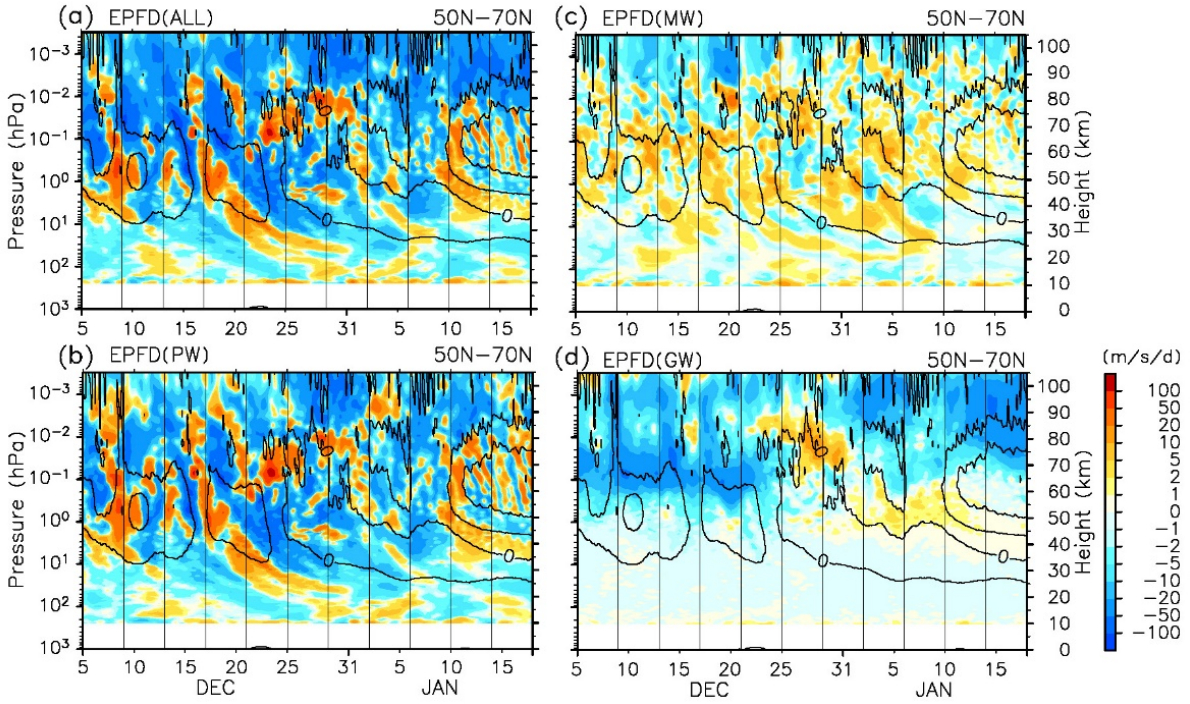


**Figure 2**. Time–height sections of EPFD averaged over 50° N–70° N of (a) all wave components, (b) PW, (c) MW, and (d) GW (colors) and $[u]$ averaged over 50° N–70° N (contour interval: 20 m $s^{-1}$). Vertical lines represent the boundaries of the model runs.

The stratopause begins to descend from a climatological height of $z$= ~55 km in association with the SSW around 22 December 2018 (Figs. 1c, 1d and 1e). Zonal mean zonal winds $[u]$ are reversed in the region of $z$= 40–80 km around 25 December (Fig. 1a). Following that, the stratopause and the peak of westward wind gradually descend to $z$= ~35 km. A strong temperature maximum with an amplitude of 220 K is formed at $z$= ~85 km around 28 December during the descent of the stratopause. This structure is also observed in the satellite temperature (Figs. 1e and 1f). This characteristic vertical structure of temperature is referred to as a mesospheric inversion layer (MIL). After 10 January, the eastward wind is accelerated at $z$= ~65 km and the ES is at $z$= ~80 km with a peak of 230 K. The heights of the MIL and ES in the model are consistent with those indicated by the satellite temperature data (Figs. 1e and 1f) within $z$= ±5 km. The temperature peak of the MIL is located at $z$= ~90 (~90) km and the ES is at $z$= ~80 (80–85) km in the Aura MLS (SABER) data. Other temperature structures in the model results are generally consistent with the observation data as well.

Waves were divided into three components and analyzed separately: PWs having zonal wavenumber $s$ = 1–3, medium-scale waves (MSWs) having $s$ > 3 and total horizontal wavenumber $n$< 21 and GWs having $n$= 21–639. Figure 2 shows the time–height sections of EP flux divergence (EPFD) for respective wave components. The EPFD was smoothed with a

lowpass filter with a cutoff of one day. During 23–31 December including the period when the MIL is present, GWF is strongly positive in the region of $z$= 65–90 km. Around the time of the formation of the MIL, PWF is strongly negative (~−50 m s$^{-1}$ d$^{-1}$ above $z$= 83 km). This negative PWF is physically consistent with warming at the pole and MIL formation. Around 10 January when the ES is formed, GWF and PWF are negative above $z$= 70 km and 80 km, respectively, suggesting that both negative wave forcings are responsible for ES formation. The sources of PWs responsible for the formation of the MIL and subsequent ES are discussed in detail in section 4. Because forcing by MSWs is always weak at any height or time, the following sections focus only on PWF and GWF.

### 3.2 Longitudinal structure of the MIL and ES

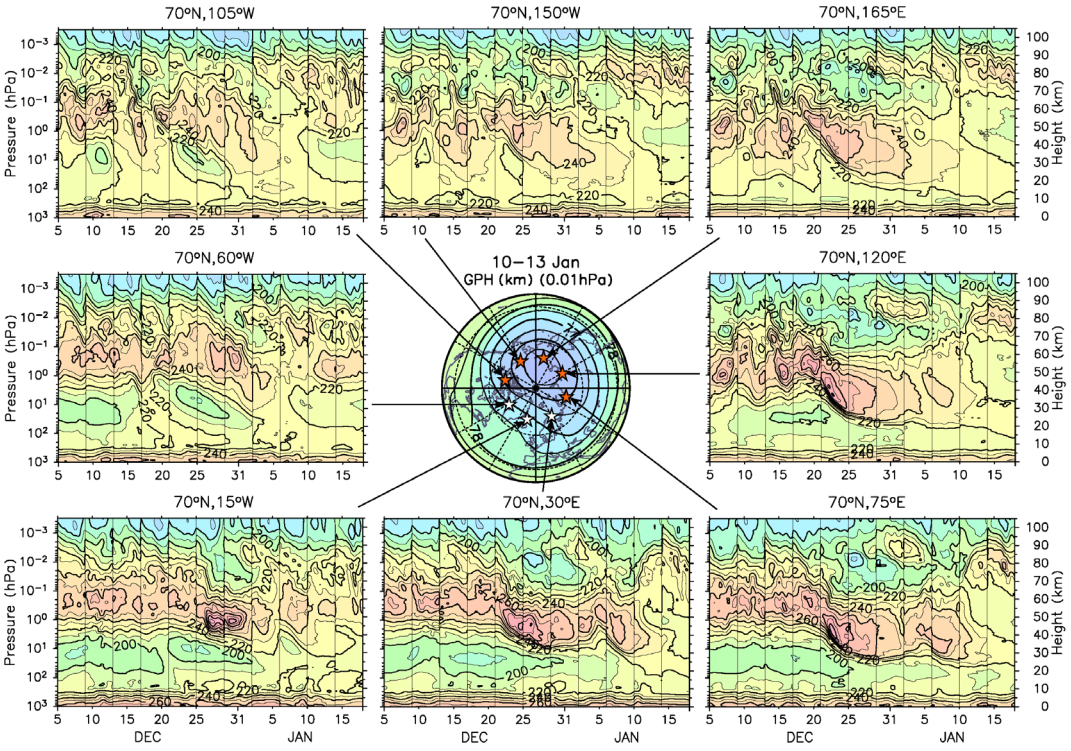


**Figure 3**. An orthographic projection map of the Northern Hemisphere showing 4-day mean GPH (unit: km) at 0.01 hPa for 10–13 January 2019 and time–height sections of $T$ (unit: K) smoothed with a lowpass filter with a cutoff of one day at a latitude of 70° N and longitudes of 30° E, 75° E, 120° E, 165° E, 150° W, 105° W, 60° W and 15° W. Star symbols in the GPH map denote the locations for the $T$ figures. Orange stars show the stations at which the ES appears clearly at $z$= ~80 km. Vertical lines in the $T$ figures represent the boundaries of the model runs.

As shown in previous studies (e.g., France & Harvey, 2013), the ES often has zonal asymmetry. To examine the longitudinal structure of the MIL and ES, the time-height sections

at stations arranged along a latitude of 70° N at a fixed longitudinal interval of 45° are shown in Fig. 3. The MIL is clearly observed at 15° W, 30° E, 75° E, 120° E, 165° E and 150° W. The ES is observed at 75° E, 120° E, 165° E, 150° W and 105° W. Figure 4 shows the orthographic maps of geopotential height (GPH) at the MIL (0.005 hPa) and ES altitudes (0.01 hPa) for the periods in which they were observed. In addition to the model results, MLS and SABER observations are shown. Note that the SABER data in Fig. 4c is for 28 December 2018 because the SABER switched to the observation in a northward-viewing yaw on 27 December 2018. The model-simulated structure and location of the polar vortex agree with the satellite observations for each case. The stations where the MIL or ES appear clearly, denoted by orange stars in Figs. 4a and 4b, are located inside of the polar vortex. Thus, it is indicated that the MIL and ES are not an apparent phenomenon that is only seen in the zonal mean field associated with a shift of the polar vortex but is a real warming of the atmosphere inside of the polar vortex.

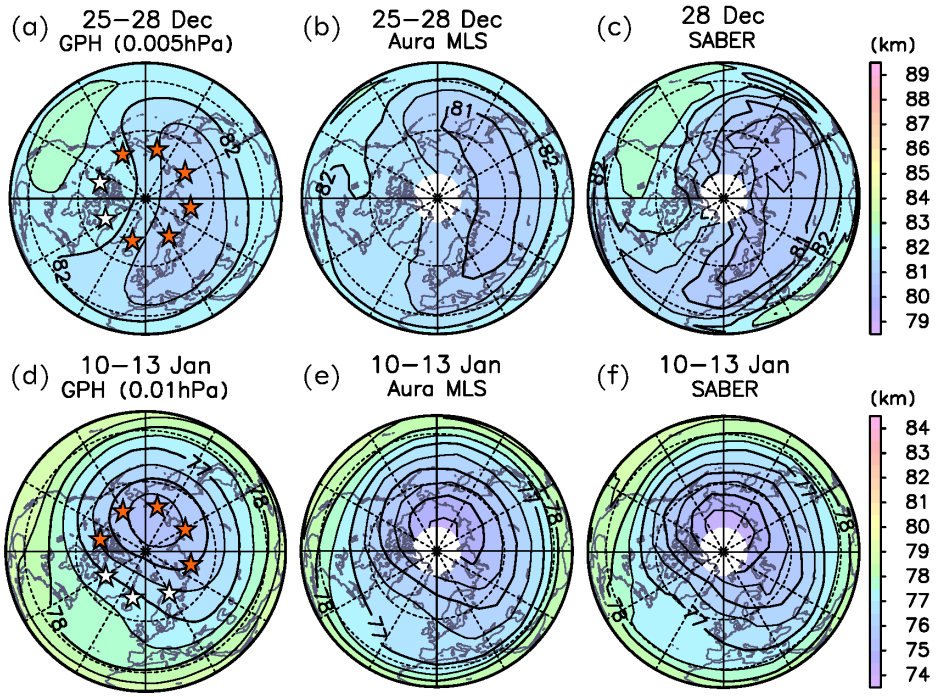


**Figure 4**. Orthographic projection maps of GPH at 0.005 hPa from (a) the JAGUAR and (b) Aura MLS for 25–28 December 2018 and from (c) the SABER for 28 December, and at 0.01 hPa from (d) the JAGUAR, (e) Aura MLS and (f) SABER for 10–13 January 2019. Stars in Figs. 4a and 4d represent the locations for the $T$ figures in Fig. 3. Orange stars show the stations at which the MIL or ES appears clearly.

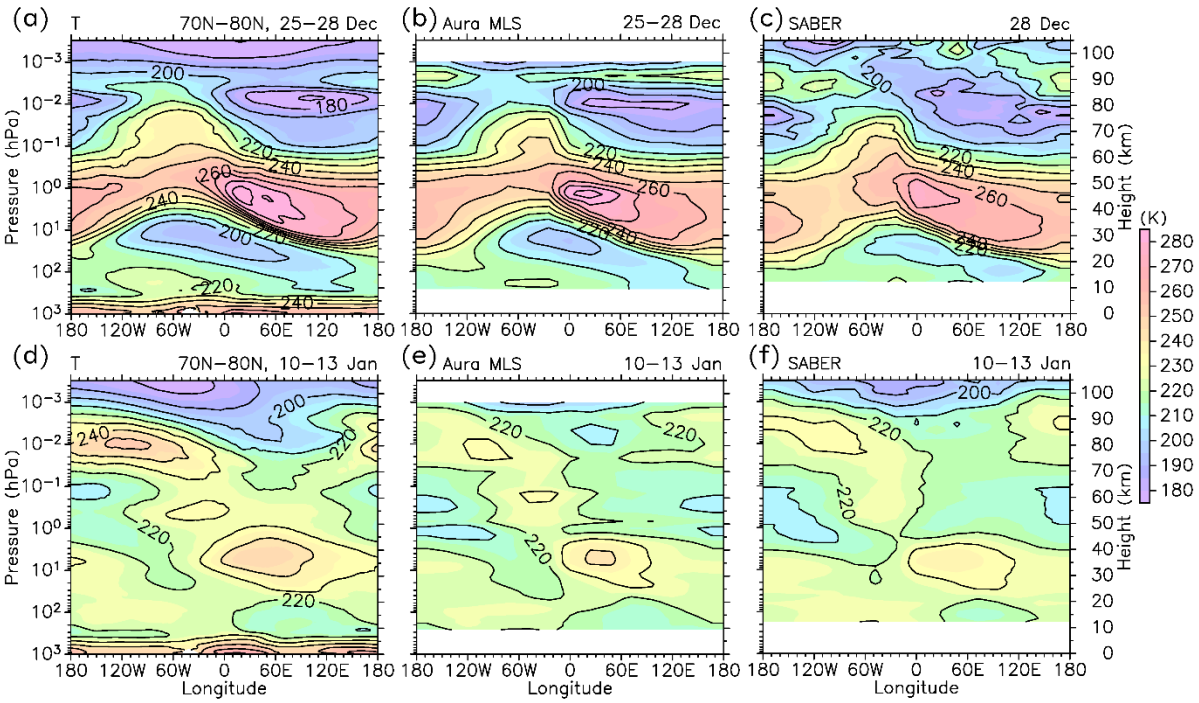


**Figure 5**. Longitude-height sections of $T$ averaged over 70° N–80° N from (a) the JAGUAR and (b) Aura MLS for 25–28 December 2018 and from (c) the SABER for 28 December 2018, and from (d) the JAGUAR, (e) Aura MLS and (f) SABER for 10–13 January 2019.

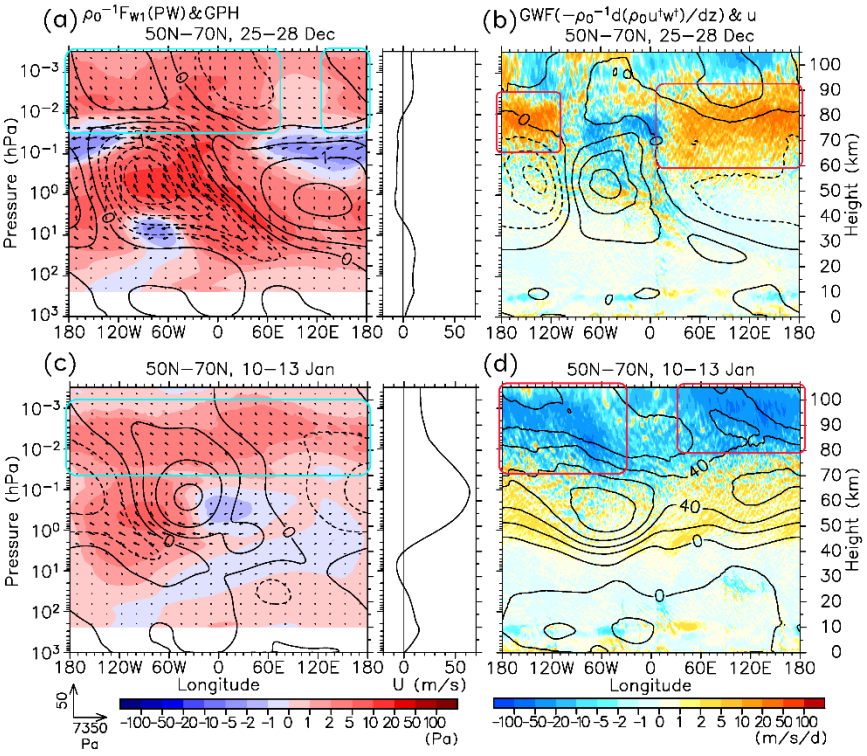


**Figure 6**. Longitude-height sections at 50° N–70° N of (a, c) 3D-flux-W (vectors, colors: vertical components) and GPH anomaly from the zonal mean (contour interval: 1 km) and (b, d) GWF and $u$ (contour interval: 10 m s$^{-1}$) for (a, b) 25–28 December 2018 and (c, d) 10–13 January 2019. The right panels in Figs. 6a and 6c show the $[u]$ profiles.

Figure 5 shows the longitude-height sections at 70° N–80° N of temperature during the MIL and ES formation. The MIL appears in a thin layer at $z$= ~90 km in a longitude region of 100° E–180°–0° (Fig. 5a), which is consistent with the SABER observation (Fig. 5c). The ES is observed at $z$= 75–85 km with slight dependence on the longitude (Fig. 5d). This structure is consistent with the MLS and SABER (Figs. 5e and 5f). The temperature maximum of the ES is ~250 K at $z$ = ~80 km, 120° W. The longitude-height structure of PW propagation represented by 3D-flux-W and GWF $-\rho_0^{-1}d(\rho_0 u^{\dagger}w^{\dagger})/dz$, where † denotes the GW components, during the MIL formation are shown in Figs. 6a and 6b. Positive GWF is observed above the westward $u$ (red boxes in Fig. 6b). The longitudinal distribution of GWF is consistent with the cold region at $z$= 60–85 km (Figs. 5a–5c) considering the downward control principle (Haynes et al., 1991). PWs propagating from the lower atmosphere are mostly attenuated below $z$= 70 km. This is likely due to the nearly zero or westward $[u]$ at $z$= 40–80 km (the right panel in Fig. 6a). According to the Charney and Drazin theorem (1961), PWs cannot propagate upward in a westward wind. However, above $z$= 75 km, strong upward PW propagation is observed at longitudes where the $T$ peak of the MIL is observed, which is denoted by cyan boxes in Fig. 6a.

Figs. 6c and 6d are the same as Figs. 6a and 6b but for the ES formation. Upward propagating PWs appear at $z$= 70–100 km at almost all longitudes. GWF is strongly negative at longitudes of 30° E–180°–30° W (red boxes in Fig. 6d). This is because the polar night jet has recovered and flow is eastward in this longitude sector (black contours). The ES has similar longitudinal structure (Figs. 5d–5f). Thus, it is inferred that this GWF distribution is responsible for the ES longitudinal structure, which is consistent with the suggestion in France and Harvey (2013). Note also that the PWs from the lower atmosphere cannot reach above $z$= ~35 km where $[u]$ is westward.

The characteristics of the MIL in this event differ significantly from those reported by previous studies. Meriwether and Gerrard (2004) reviewed the two types of MILs, namely "upper" and "lower" MILs. An upper MIL is typically observed at $z$= 85–100 km and formed by tidal waves. The interaction between tidal wave and gravity wave intensifies this type of MIL. Thus, the upper MILs should be washed out in daily mean (Meriwether & Gardner, 2000). A lower MIL is observed at $z$= 65–80 km and formed by PWs. When a PW is strongly attenuated below its critical layer, which is caused by GWF, $T$ anomaly due to $\Phi'_z$ of the PW forms a MIL (Salby et al., 2002; Sassi et al., 2002; France et al., 2015).

The MIL in this SSW ES event appears at a similar altitude to typical upper MILs (Fig. 1c). However, it kept its strength for ~9 days and does not have significant dependence on the local time (not shown). The longitude-height structure of GPH anomaly and 3D-flux-W for PWs is shown in Fig. 7. At most longitudes, except for ~60° W, PWs from the lower atmosphere are strongly attenuated at $z$= 40–60 km where $[u]$ is westward. However, large $\Phi'_z$ due to

the PWs is not fully observed over the longitude range of the MIL. Therefore, it is suggested that this MIL formation is not explained by the mechanisms discussed by previous studies, but due to adiabatic heating associated with $\bar{w}^*$ induced by wave forcing as discussed above.

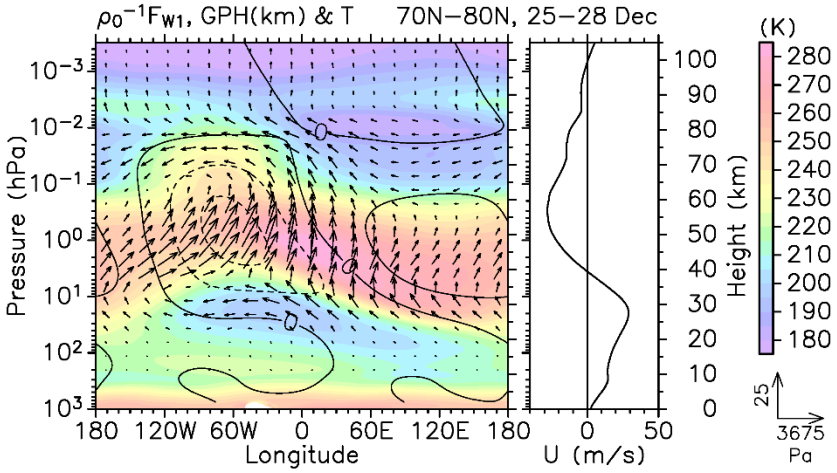


**Figure 7**. 3D-flux-W (vectors) and GPH anomaly associated with $s$ = 1–3 component (contours, interval: 1 km) at 50° N–70° N. Colors represent $T$ shown in Fig. 5a. The right panel shows the $[u]$ profile.

## 4 Sources of mesospheric PWs during the MIL and ES formation

Both in the MIL and subsequent ES formation, PWs from the lower atmosphere hardly reach the MLT. Thus, the sources of PWs which contribute to the formation of the MIL and ES are examined in this section.

### 4.1 The formation of the MIL during 25–28 December 2018

#### 4.1.1 Meridional cross sections

Figure 8 shows the meridional cross sections of zonal mean and four-day mean fields of temperature, zonal wind, MPV, and EP flux and EPFD of PWs and GWs for 17–20, 21–24 and 25–28 December 2018 and 2–5 January 2019. The MIL appears around 28 December (Fig. 1c). To accentuate vectors in the middle atmosphere, EP flux vectors are divided by $\rho_0 a$ in all the figures. From 17–20 December, there is a strong eastward polar night jet, and its axis is at ~50° N and $z$= ~52 km (contours in Fig. 8c or 8d). Westward wind is observed equatorward of this eastward jet. GWF is strongly negative up to ~50 m s$^{-1}$ d$^{-1}$ at ~50° N and $z$= ~65 km above the eastward jet, and positive above the westward wind region (Fig. 8d). These GWF patterns are due to the filtering effect by the eastward and westward mean wind below.

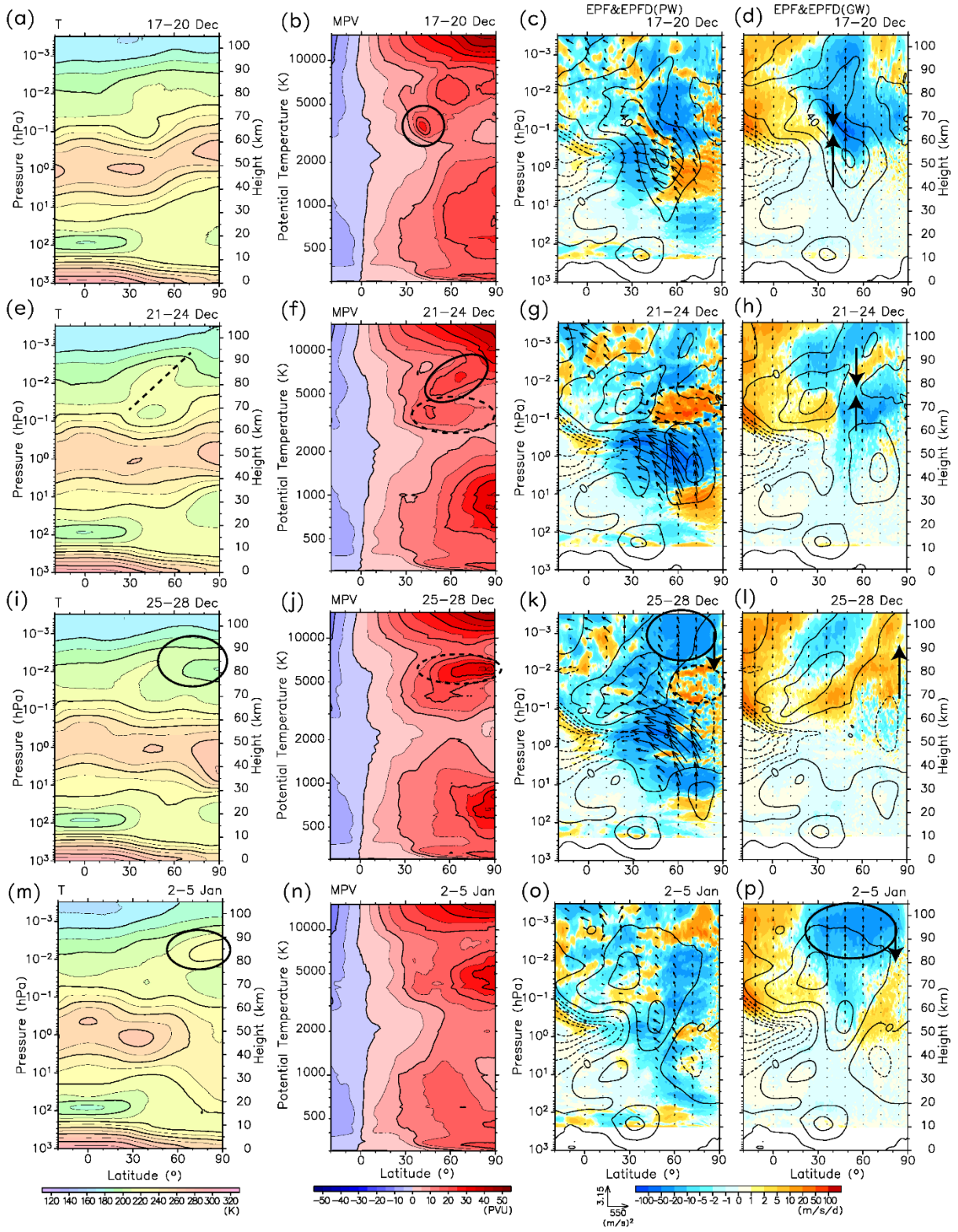


**Figure 8**. Latitude–height sections of (from left to right) 4-day mean $[T]$, $[P_M]$ and EP flux scaled by $\rho_0 a$ (vectors) and EPFD (shadings) of PWs and GWs for (a-d) 17–20, (e-h) 21–24, and (i-l) 25–28 December 2018 and (m-p) 2–5 January 2019. Contours in the figures of EP flux and EPFD denote $[u]$ (contour interval = 20 m $s^{-1}$).

415

416 There is a notable peak of $[P_M]$ at ~40° N and $\theta$= ~3,500 K ($z$= ~65 km) (shown by
417 the solid circle in Fig. 8b), where the GWF is negative poleward and positive equatorward from
418 17–20 December (Fig. 8d). Generally, wave-induced residual mean vertical wind $\overline{w}^*$ is
419 upward in the lower region on the poleward (equatorward) side of positive (negative) wave
420 forcing (not shown, denoted by the lower arrow in Fig. 8d). Above this region, downward $\overline{w}^*$
421 was observed (the upper arrow in Fig. 8d). This $\overline{w}^* < 0$ seems due to tilted distribution of
422 negative GWF which spread equatorward above this $\overline{w}^*$<0 region. These GWF and $[P_M]$
423 features suggest that the $[P_M]$ peak is a result of an increase in $N^2$ due to the convergence of
424 $\overline{w}^*$ at ~40° N induced by GWF.

425 During 17–20 December, PWF is positive poleward of ~55° N at $z$= 35–55 km. PW
426 packets propagate toward the region with weak $[u]$ at ~30° N, $z$= 40–65 km and toward 40°
427 N–70° N, $z$= 60–85 km by way of the eastward jet, which has its axis at ~50° N, $z$= ~52 km
428 (Fig. 8c). In both regions, PWF is negative. The negative PWF in the latter region may also
429 contribute to the upwelling at ~40° N and the increase in $N^2$ and $[P_M]$. However, the
430 boundary of the positive and negative total wave forcing (not shown) matches well with that
431 of the positive and negative GWFs. Thus, the location and strength of the $\overline{w}^*$ are mainly
432 determined by the GWFs.

433 During 21–24 December, the eastward jet is split into two segments (Fig. 8g or 8h).
434 One segment is shifted poleward and downward and located at ~72° N, $z$= ~42 km and the
435 other segment is tilted poleward from the equator at $z$= ~65 km to the winter pole at $z$= ~100
436 km with its axis at ~25° N, $z$= ~72 km. This segmentation of the jet may be caused by negative
437 GWF and PWF that are present during 17–20 December in the region where the split occurs
438 (Figs. 8c and 8d). During 21–24 December, GWF is negative (positive) above (below) the latter,
439 poleward-tilted eastward jet. It is consistent with the GW filtering effect of this jet (Fig. 8h).
440 Most PWs are refracted equatorward below $z$= 60 km (Fig. 8g). The temperature cross section
441 shows relatively high temperature between 30° N, $z$= ~70 km and 70°N, $z$= ~95 km, denoted
442 by the dashed line in Fig. 8e. This temperature peak spread over nearly all longitudes with
443 height variation from 70–90 km (not shown). This warm layer corresponds to the area between
444 the negative and positive GWFs along the mesospheric jet. This fact suggests that the high
445 temperature is caused by adiabatic heating associated with residual mean downwelling (not
446 shown, denoted by the downward arrow in Fig. 8h) induced by these GWFs.

447 Poleward of 10° N in the middle and upper stratosphere at $z$= 35–60 km during 21–24
448 December, PWF is strongly negative with a maximum of over 50 m $s^{-1}$ $d^{-1}$ and is present
449 continuously until 25–28 December (Fig. 8k). It is inferred that the SSW is caused by this PWF.
450 During 21–24 December, PWF is positive to the north of ~40° N at $z$= 60–80 km (Fig. 8g),
451 and the $[P_M]$ peak that is present during 17–20 December at ~40° N and $\theta$= ~3,500 K

becomes weak (Fig. 8f). According to the quasi-geostrophic theory, a positive EPFD is equivalent to a poleward PV flux, while a negative EPFD indicates an equatorward PV flux (e.g., Andrews et al., 1987). The observed PWF features suggest that the positive wave forcing is associated with the PW generation due to the BT/BC instability weakening the negative $[P_M]_y$, which is a necessary condition for the BT/BC instability. During this period, a $[P_M]$ peak becomes obvious from ~50° N, $\theta$= ~5,500 K ($z$= ~80 km) to ~80° N, $\theta$= ~7,000 K ($z$= ~85 km, Fig.8f). It is slightly below the region with relatively high temperature, which is marked by the dashed line in Fig. 8e. Thus, it is implied that this $[P_M]$ peak is caused by the increase of $N^2$ under the temperature maximum associated with the isothermal folding.

During 25–28 December, a westward jet with a peak at $z$= ~57 km, ~80° N is formed in the polar upper stratosphere and mesosphere (Fig. 8k or 8l). The stratopause shifts downward from $z$= ~52 km in 21–24 December to $z$= 38 km corresponding to the SSW (Fig. 8i). A relatively weak maximum in the vertical profile of $[T]$ is formed to the north of 60° N at $z$= ~88 km. This structure is the MIL. Poleward of 55° N at $z$= 67–82 km, where the $[P_M]_y$ is negative in 21–24 December (Fig. 8f), PWF becomes positive during 25–28 December (Fig. 8k) and the $[P_M]_y$< 0 region almost disappears (Fig. 8j). These results suggest in-situ PW generation due to BT/BC instability at $z$= 67–82 km during 25–28 December, which is similar to the situation at > 40° N, $z$= 60–80 km from 21–24 December.

During 25–28 December, a negative PWF of $\sim -20$ m s$^{-1}$ d$^{-1}$ extends to the north of 35° N above $z$= 85 km (Fig. 8k), and a positive GWF of ~10 m s$^{-1}$ d$^{-1}$ is in the polar MLT (Fig. 8l). Because the positive GWF is weaker than the negative PWF, the total wave forcing is negative in the polar MLT ($z$> 80 km) (Fig. 2a), which cause downwelling in the polar MLT and the subsequent adiabatic heating. Thus, it is considered that the initial formation of the MIL is caused by PWF.

During 25–28 December, $[u]$ is westward over a wide area above $z$> 40 km in the polar upper stratosphere and mesosphere. PWs from the lower atmosphere are strongly refracted equatorward below this area as indicated by EP flux vectors in Fig. 8k, which can be suggested by the attenuation of the vertical component of 3D-flux-W in Fig. 6a as well. Thus, it is inferred that PWs responsible for the MIL formation originate from the BT/BC instability during 17–20 and/or 21–24 December. Afterwards, GWF from 2–6 January is strongly negative in the MLT (Fig. 8p). Downwelling induced by this GWF likely intensify the amplitude of the MIL (Fig. 8m).

#### 4.1.2 Three-dimensional structure

In addition to the discussion above about zonal mean fields, the three-dimensional structure of $P_M$ and wave forcing is also analyzed in this section. Orthographic projection

maps of the Northern Hemisphere for $P_M$, GPH and $N^2$ at $\theta$= ~3,500 K and 0.1 hPa ($z$= ~65 km) during 17–20 December are shown in Figs. 9a and 9b. A strip of high $P_M$ at ~40° N (Fig. 9a), which corresponds to the region of $[P_M]$ maximum in Fig. 8b, matches with the region of high $N^2$ (Fig. 9b) and does not match with the region of the center of the polar vortex in the GPH maps (Fig. 9a). This $P_M$ peak along the edge of the polar vortex is consistent with the result by Harvey et al. (2009). The latitude-height sections along a longitude of 90° E of $N^2$, $T$, GWF, $u$ and $\overline{w}^*$ are shown in Figs. 9c and 9d. The blue (red) hatched areas represent regions of $\overline{w}^*$< (>) $-2$ cm s$^{-1}$. GWF and $\overline{w}^*$ were zonally smoothed with a lowpass filter with a cutoff of $s$= 6 to show large-scale structures more clearly. High $N^2$ in Fig. 9c appears where $\overline{w}^*$ converges, i.e., $\overline{w}^*$ is upward below and downward above, along with the equatorial side of negative GWF in Fig. 9d. These features indicate that the $[P_M]$ enhancement in the zonal mean field (Fig. 8b) is mainly caused by $N^2$ increase in the region of $\overline{w}^*$ convergence induced by GWF, which is similar to the mechanism shown by Sato and Nomoto (2015).

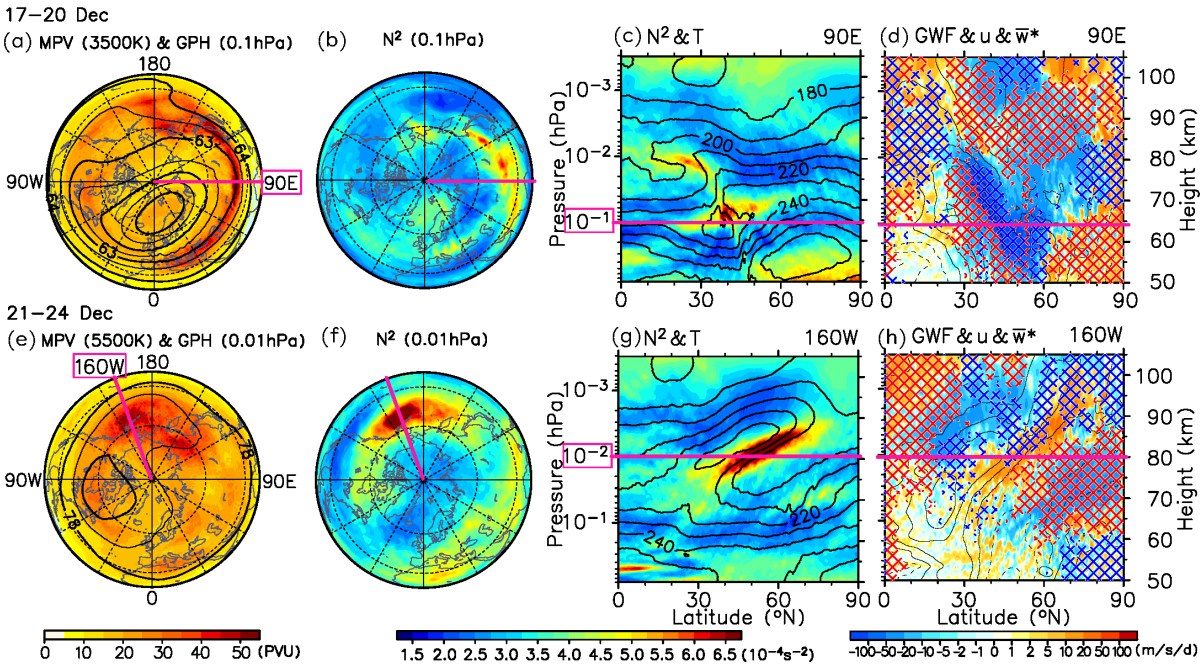


**Figure 9**. Orthographic projection maps of the Northern Hemisphere of (a, e) $P_M$ and GPH and (b, f) $N^2$ at (a, b) 0.1 hPa and $\theta$= 3,500 K ($z$= ~65 km) for 17–20 December 2018 and (e, f) 0.01 hPa and $\theta$= 5,500 K ($z$= ~80 km) for 21–24 December 2018. (c, g) $N^2$ (colors) and $T$ (contours, interval: 10 K) (d, h) GWF (colors), $u$ (contours, interval: 10 m s$^{-1}$) and $\overline{w}^*$ (cross-hatched, red: $\overline{w}^*$> 2 cm s$^{-1}$, blue: $\overline{w}^*$< $-2$ cm s$^{-1}$) at longitudes of (c, d) 90° E for 17–20 December and (g, h) 160° W for 21–24 December. GWF and $\overline{w}^*$ have been zonally smoothed with a lowpass filter with a cutoff of s= 6.

Figures 9e–9h are the same as Figs. 9a–9d but for 21–24 December at $\theta$= ~5,500 K

and 0.01 hPa ($z$= ~80 km) and at 160° W, the longitude where the $P_M$ and $N^2$ peaks. Similar to the period of 17–20 December, the region of high $P_M$ at ~50° N, 120° E–120° W roughly corresponds to the region of high $N^2$. This $N^2$ peak is observed along the bottom of an isothermal folding in Fig. 9g. This folding well corresponds to the distribution of $\overline{w}^*$. GWF has a tilted structure along with the mesospheric jet. The distribution of $\overline{w}^*$ is consistent with the GWF considering the downward control principle. Thus, it is inferred that the features observed in these maps support the inference from the zonal mean fields that the $P_M$ peak is formed as a result of $N^2$ increase induced by the GW-driven $\overline{w}^*$ convergence.

### 4.2 The formation of the ES during 10–13 January 2019

#### 4.2.1 Meridional cross sections

To examine the mechanism of ES formation, latitude–height sections of $[T]$, $[u]$, $[P_M]$ and EP flux and EPFD of PWs and GWs after the SSW onset on 1 January for the time periods of 6–9 and 10–13 January are shown in Fig. 10. The ES becomes visible at $z$= ~80 km to the north of 70° N during 10–13 January (Fig. 10e).

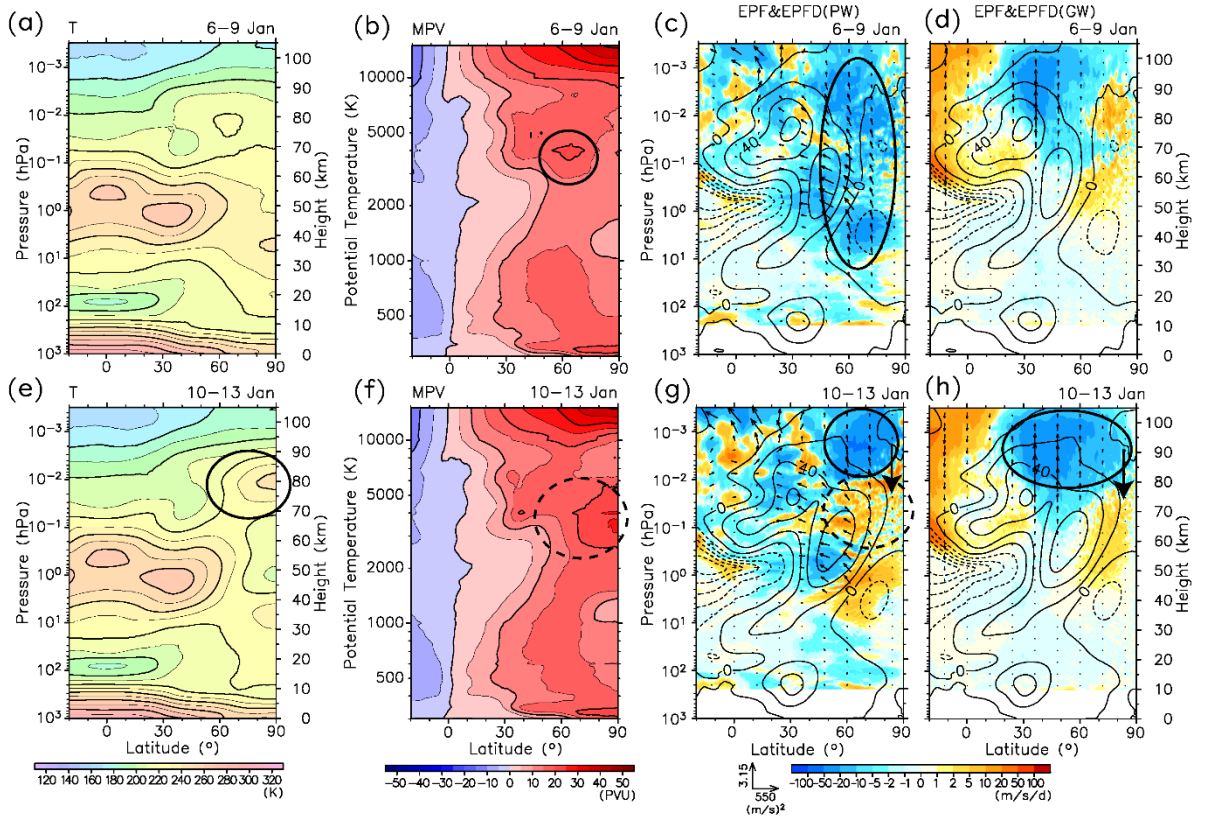


**Figure 10**. Same as Fig. 8 but for (a–d) 6–9 and (e–h) 10–13 January 2019.

During 6–9 January, the prevailing PWF through the entire winter polar middle

atmosphere is negative with values of about $-10$ to $-20$ m s$^{-1}$ d$^{-1}$ (Fig. 10c). After the SSW onset, westward wind has descended to the stratosphere, and is reinforced during 6–9 January (Fig. 1a). Thus, it is implied that the prevailing mesospheric westward wind during this period is caused by this negative PWF. In the $[P_M]$ cross section in Fig. 10b, there is a peak at ~60° N and $\theta$= 3,000–6,000 K (z= 60–80 km) denoted by a solid circle.

The negative or near zero $[P_M]_y$, which is poleward of ~60° N and over the wide region of $\theta$= 500–6,000 K ($z$= 22–80 km) during 6–9 January (Fig. 10b), has disappeared from $\theta$= 1,200–6,000 K ($z$= 40–80 km) in 10–13 January (the dashed circle in Fig. 10f). During 10–13 January, PWF is strong and positive poleward of 60° N at $z$= 35–80 km (Fig. 10g). This region of positive PWF roughly matches the region where the negative $[P_M]_y$ in 6–9 January becomes positive in 10–13 January. These features suggest in-situ PW generation due to the BT/BC instability.

As seen in contours of Fig. 10g or 10h, during 10–13 January, the eastward jet becomes stronger and extends to the polar mesosphere. The PWs and GWs provide strong negative forcing at $z$> 80 km poleward of 50° N and 20° N, respectively (Figs. 10g and 10h). There is a $[T]$ maximum corresponding to the ES poleward of ~60° N at $z$= ~80 km. Thus, it is considered that both negative PWF and GWF are responsible for the ES formation by causing downwelling below and poleward of the forcing regions. As discussed in section 3.2 (Fig. 6c), PWs from the lower atmosphere hardly reach the MLT during 10–13 January. Thus, it is inferred that the in-situ generated PWs contribute to the ES formation.

During 6–9 January, PWF is observed in the mesosphere despite the westward wind in the polar stratosphere. The longitude-height sections of 3D-flux-W $\rho_0^{-1}\mathbf{F}_{W1}$ averaged over 60° N–70° N for 6–9 January are shown in Fig. 11. The vectors represent the zonal and vertical components of the flux, the colors represent the vertical components of $\rho_0^{-1}\mathbf{F}_{W1}$ and the contours represent the zonal wind averaged over 60° N–70° N at each longitude. The upward propagation of PWs occurs mainly in the region of 60° W–60° E, where the zonal wind has a westward-tilted structure at $z$= 20–55 km. This structure is consistent with that of upward propagating PWs and similar situation was observed during the major SSW in February 2018 (e.g., Harada et al., 2019). Thus, the westward winds in this region can be regarded as part of the PWs. It is inferred that PWs propagate upward in the region of 60° W–60° E, even though $[u]$ is westward.

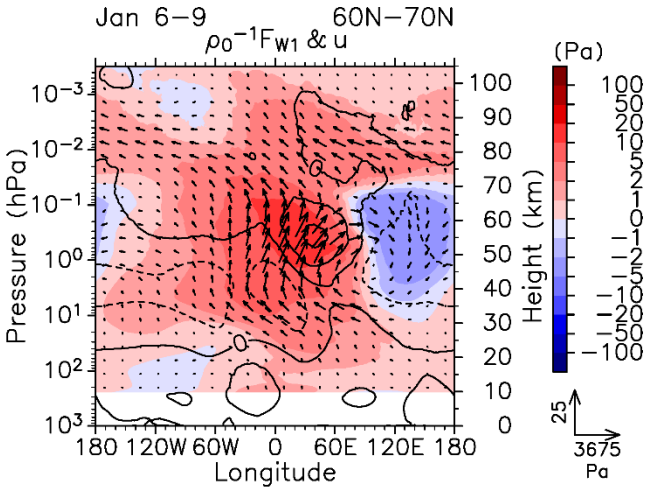


561

562 **Figure 11**. Longitude–height section of the 3D-flux-W $\mathbf{F}_{w1}$ weighted by $\rho_0^{-1}$ (colors and
563 vectors) averaged over 60° N–70° N for 6–9 January 2019. Colors indicate the vertical
564 component of $\rho_0^{-1}\mathbf{F}_{w1}$. Contours indicate $u$ averaged over the same region (contour interval
565 = 20 m s$^{-1}$). Dashed contours indicate negative values.

566

567 4.2.2 Horizontal structure

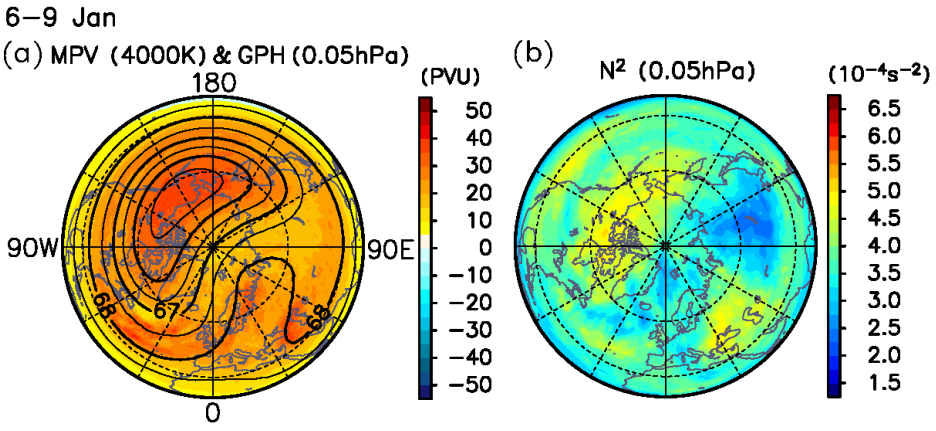


568

569 **Figure 12**. Orthographic projection maps of the Northern Hemisphere showing 4-day mean
570 (left to right) $P_M$, GPH and $N^2$ at 0.05 hPa and $\theta$= 4,000 K ($z$= ~70 km) for 6–9 January
571 2019.

572

573 To examine the formation of the $[P_M]$ peak at ~60° N, $\theta$= 3,000–6,000 K ($z$= 60–80
574 km) during 6–9 January in terms of the horizontal structure, orthographic projection maps of
575 $P_M$, GPH and $N^2$ at $\theta$= ~4,000 K and 0.05 hPa ($z$= ~70 km) are shown in Fig. 12. In contrast
576 to the results from 17–20 and 21–24 December (Fig. 4), high $P_M$, low GPH (i.e., the center of
577 the polar vortex) and high $N^2$ appear roughly in the same regions. The polar vortex is shifted

equatorward at ~135° W. This shift of the polar vortex is consistent with the MLS and SABER observations (not shown). The region of low GPH is stretched and distorted into a comma-like shape at ~60° E. This is a typical structure for PW breaking. Thus, it is inferred that the mixing caused by PW breaking eliminates the expected $P_M$ minimum at ~60° E associated with the phase of the PWs which had to be observed without breaking, and only the $P_M$ maximum at ~135° W remains.

## 5 Characteristics of PWs and GWs

### 5.1 Characteristics of PWs generated in the middle atmosphere

To examine the PW periods, the longitude–time section of GPH deviation from zonal mean at 60° N–70° N, $z$= 80 km is shown in Fig. 13. During 21–24 December, when positive PWF appears north of ~40° N at $z$= 60–80 km (Fig. 8g), stationary PWs with $s$= 1 are dominant. During 25–28 December, when PWF is positive poleward of 55° N at $z$= 67–82 km and the MIL is formed (Fig. 3c), westward propagating PWs have periods of ~6 days (indicated by the dashed line in Fig. 13) and wavenumbers of $s$= 1–2. During 10–13 January, when positive PWF is observed poleward of 60° N at $z$= 35–80 km, PWs have periods of ~24 days (the dash-dotted line) and wavenumbers of $s$= 1.

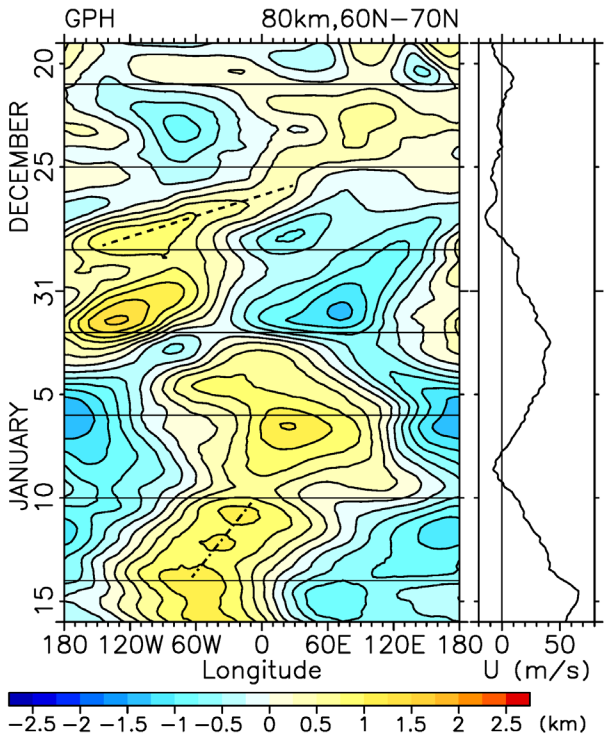


**Figure 13**. Left panel: longitude–time section of GPH anomaly from zonal mean averaged over 60° N–70° N, $z$= 80 km. Thin horizontal lines represent the boundaries of the model runs. A dashed line and a dash-dotted line denote propagations with periods of 6 days and 24 days,

599 respectively. Right panel: variations with height of $[u]$ averaged over the same latitudinal
600 region.
601

602 5.2 Propagation of GWs

603 To examine the contribution of GWs which are generally ignored in GW
604 parameterizations, the GWs which play crucial roles in the formation of the MIL and ES are
605 further analyzed. Figure 14 shows the vertical flux of zonal momentum $[u^{\dagger}w^{\dagger}]$ of GWs as a
606 function of the ground-based phase velocity $c$ at each height. The solid and dashed curves
607 denote the mean $[u]$ and $[u] \pm 1.65\sigma$ over a 20° latitude range centered around 50° N (Fig.
608 14a), 30° N (Fig. 14b), 60° N (Fig. 14c), and 60° N (Fig. 14d). Assuming normal distribution
609 for $[u]$, the area between each pair of dashed curves encompasses 90% of the values of $[u]$.
610 Figures 14a, 14b, 14c and 14d are the profiles for GWs at 50° N for 17–20 December (Case
611 A), 30° N for 21–24 December (Case B), 60° N for 2–5 January (Case C) and 60° N for 10–13
612 January (Case D), respectively. As discussed in section 4.1, it is likely that in Cases A and B,
613 GWs are responsible for the $[P_M]$ peaks that appear before the formation of the MIL. The GW
614 momentum flux in Case C is likely related to the reinforcement of the MIL structure after SSW
615 onset. In case D, GWs exert strong negative forcing in the MLT during the formation phase of
616 the ES.

617 The vertical flux of zonal momentum $[u^{\dagger}w^{\dagger}]$ for Case A (Fig. 14a) is strongly
618 negative around $c$= ~0 m s$^{-1}$ at all altitudes. At its strongest, its absolute value exceeds ~0.1
619 m$^2$ s$^{-2}$. In Cases B, C and D, the negative $[u^{\dagger}w^{\dagger}]$ peaks around $c$= ~0 m s$^{-1}$ in the troposphere
620 and the lower stratosphere are absent in the upper stratosphere. This is likely because of weak
621 wind layers in the lower or middle stratosphere.

622 In Case B, there is a weak wind layer with $[u]$= $\pm$10 m s$^{-1}$ at $z$= 20–55 km; in addition
623 to the small $[u]$, the variation of $[u]$, as indicated by the area between the two dashed lines is
624 also small at $z$= 20–30 km. In Cases C and D, the weak wind layers of $[u]$= $\pm$10 m s$^{-1}$ are at
625 $z$= 25–50 km and $z$= 20–45 km, respectively. Because the meridional wind is generally weaker
626 than $[u]$ and the meridional component of the ground-based phase velocity of a GW is smaller
627 than the zonal component in most cases, GWs having $c$= ~0 m s$^{-1}$ such as orographic waves
628 break down at a critical layer, a layer with $[u]$= ~0 m s$^{-1}$. However, $[u^{\dagger}w^{\dagger}]$ of GWs having
629 $c$= ~0 m s$^{-1}$ above these layers is strongly negative at $z$= 65–100 km in Case B, $z$> 47 km in
630 Case C and $z$> 55 km in Case D. The lowest values of $[u^{\dagger}w^{\dagger}]$ are ~$-1\times10^{-2}$ m$^2$ s$^{-2}$ at $z$=
631 70–90 km in Case B, ~$-1\times10^{-2}$ m$^2$ s$^{-2}$ at $z$= 75–95 km in Case C and ~$-1\times10^{-2}$ m$^2$ s$^{-2}$ at $z$=
632 75–95 km in Case D. These negative momentum fluxes of GWs having $c$= ~0 m s$^{-1}$ cannot be
633 explained only by pure vertical propagation from the lower atmosphere, which is the
634 assumption that is made in most GW parameterizations. This result indicates that these waves
635 propagate from other latitudes and/or are excited in the middle atmosphere.

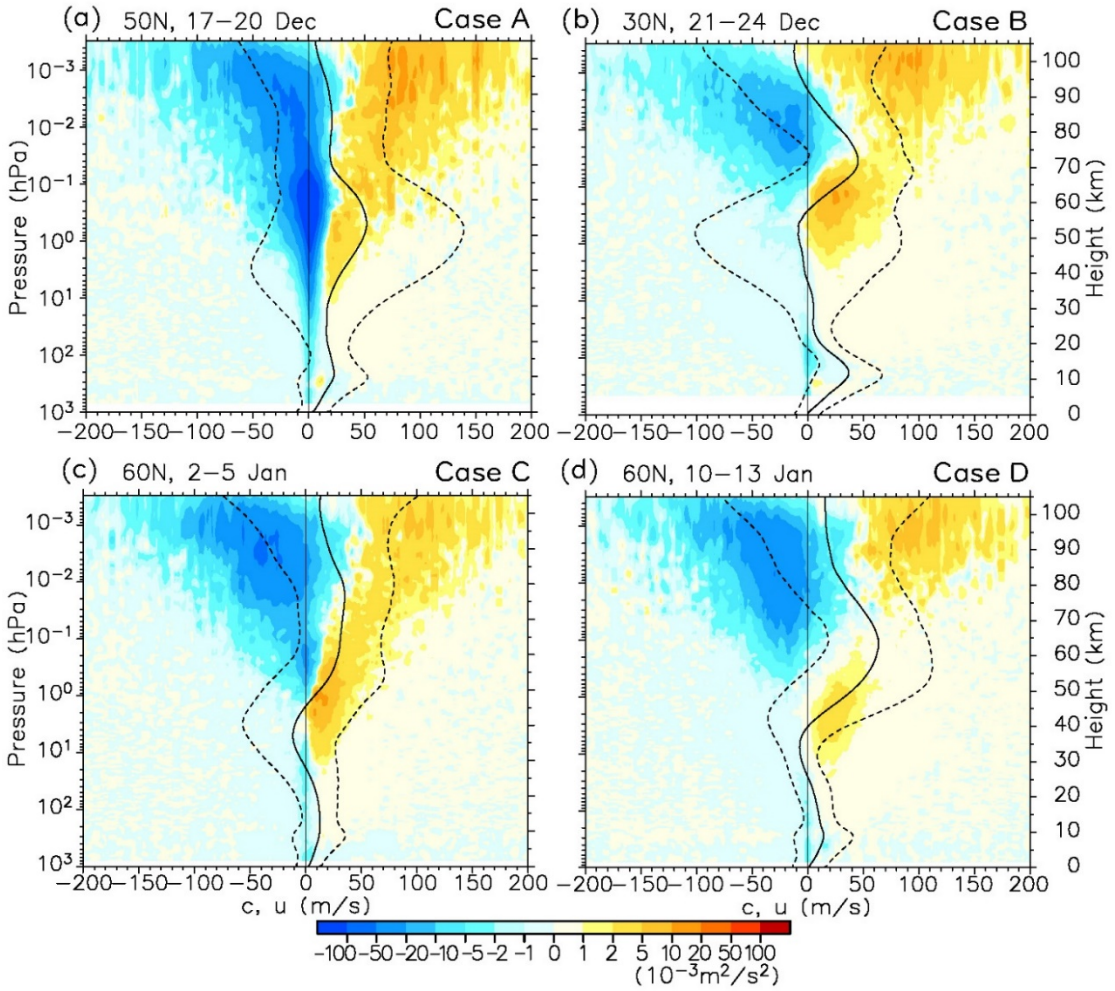


**Figure 14**. Vertical profiles of $[u^{\dagger}w^{\dagger}]$ of GWs as a function of the ground-based zonal phase velocity at each height (shading) at (a) 50° N for 17–20 December 2018 (Case A), (b) 30° N for 21–24 December 2018 (Case B), (c) 60° N for 2–5 January 2019 (Case C), and (d) 60° N for 10–13 January 2019 (Case D). The values $[u^{\dagger}w^{\dagger}]$ are smoothed by the 3-point moving average in the phase velocity direction. Solid curves denote the mean $[u]$ over a 20° latitude range centered around (a) 50° N, (b) 30° N, (c) 60° N, and (d) 60° N. Dashed curves on either side of the solid curve denote $[u]\pm1.65\sigma$, where $\sigma$ is the standard deviation. Assuming normal distribution for $[u]$, the area between each pair of dashed curves encompasses 90% of the values of $[u]$.

## 6 Summary and Conclusions

By analyzing outputs from a hindcast of the SSW ES event in 2018/19 using a GW-permitting model that covers the ground surface to the lower thermosphere, crucial importance of the interplay between PWs and GWs in the three-dimensional structure and formation of the ES and another characteristic temperature maximum observed during the event have been

652 shown quantitatively. While the heights of ESs simulated by most of the state-of-the-art high-
653 top models tend to be lower than those observed, the ES reproduced by the model used in the
654 present study appeared at a similar height to that observed by the satellites: MLS and SABER.
655 Since GWs in the model used in this study are all resolved, quantitative study including GWs
656 generated in the middle atmosphere can be carried out.

657 A characteristic temperature maximum appeared at a height of $z$= ~85 km in the polar
658 region prior to the disappearance of the lowered stratopause associated with the SSW and
659 subsequent ES onset (Figs. 1c, 1e and 1f). The existence of such a temperature maximum
660 during an SSW event has not been reported so far. This temperature maximum was observed
661 both in the model results and in the satellite observations and can be regarded as a MIL (e.g.,
662 Meriwether & Gerrard, 2004). However, the formation mechanism differs from those of the
663 MILs discussed in previous studies, as summarized in the following.

664 The MIL was observed inside of the polar vortex and its three-dimensional structure in
665 the model mostly agreed with the satellite observations. To examine the mechanism of the
666 formation, a schematic is shown in Fig. 15. Prior to the MIL formation, during 17–20 December,
667 GWF above the eastward polar night jet was strongly negative at ~50° N, $z$= ~65 km (Fig.
668 15a); GWF was positive above the westward wind at <35° N and $z$= ~65 km, equatorward of
669 the negative GWF. Because of the convergence of $\overline{w}^*$ induced by GWF, $N^2$ and thus $P_M$
670 increase at ~40° N, $z$= ~65 km.

671 During 21–24 December, negative (positive) GWF appeared above (below) the
672 eastward jet with its axis at ~25° N and $z$= ~72 km in the mesosphere. This GWF distribution
673 can be explained by a filtering effect by the mesospheric eastward jet. This jet was tilted from
674 the equatorial region in the lower mesosphere to the winter polar region in the upper
675 mesosphere. A weak temperature maximum extending toward higher altitudes and latitudes
676 was formed at the height of $\overline{w}^*< 0$, which was located between the negative and positive GWFs
677 in the mesosphere. There was also $\overline{w}^*> 0$ on the polar side of the positive GWF. Then, a $[P_M]$
678 peak caused by high $N^2$ appeared in the region of $\overline{w}^*$ convergence (Fig. 15b). Poleward of
679 this peak, $[P_M]_y$ was negative, which satisfied the necessary condition of the BT/BC
680 instability.

681 During 25–28 December, PWF was positive poleward of the $[P_M]$ peaks (Fig. 15c).
682 These features suggest that PWs were generated due to the BT/BC instability induced by the
683 GWFs. In addition, PWF in the MLT was strongly negative. This negative PWF was likely a
684 result of the PWs generated in the mesosphere because the prevailing wind was westward in
685 the stratosphere and PWs excited in the troposphere hardly propagated through into the MLT.
686 It is inferred that a downward flow induced by the negative PWF in the polar MLT caused the
687 $T$ maximum of the MIL at $z$= ~85 km. The longitudinal distribution of PWF indicated by PW
688 upward propagation in the MLT was mostly consistent with the longitudinal structure of the

MIL (Fig. 15d). The above mechanism significantly differs from that of previously reported MILs: "upper" and "lower" MILs (e.g., Meriwether & Gerrard, 2004). The MIL in this event is caused by wave-driven residual mean flow, similarly to the winter polar stratopause. Considering this mechanism and the fact that this MIL forms the second $T$ peak in the vertical along with the lowered stratopause, this morphological MIL can be also referred to as the "second stratopause".

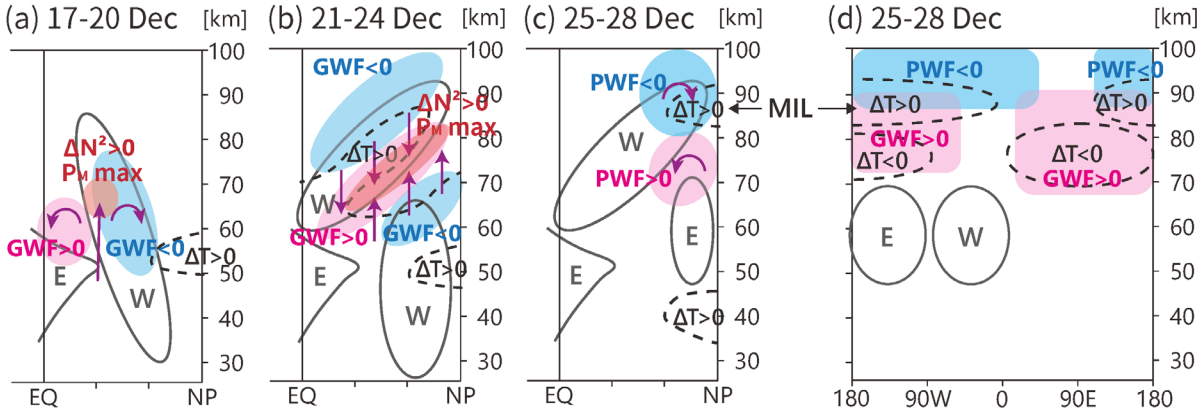


**Figure 15**. A schematic of the formation mechanism of the MIL (a–c) in the latitude–height sections and (d) in the longitude-height section; W and E denote westerly (eastward) and easterly (westward) winds; $\Delta$ represents the anomaly of each value; purple vectors indicate the residual mean flows. Note that the zonal winds, PWF and GWF are for 50° N–70° N and $\Delta T$ is for 70°N–80° N in Fig. 15d.

To examine the mechanism of the formation of the ES, a schematic is shown in Fig. 16. Then, PWF was negative throughout the entire polar middle atmosphere during 6–9 January (Fig. 16a). A $[P_M]$ maximum appeared at ~60° N and $\theta$= 3,000–6,000 K (z= 60–80 km). The orthographic projection map of $\theta$= 4,000 K ($z$= ~70 km) shows high $P_M$ inside of a comma-like polar vortex, which is a typical feature of PW breaking.

During 10–13 January, PWF was positive poleward of 60° N at $z$= 35–80 km (Fig. 16b), in a region that roughly matches the region of $[P_M]_y$< 0 in 6–9 January (Fig. 16a). These features suggest that PWs were generated in-situ by the BT/BC instability. During 10–13 January, GWF and PWF were negative at $z$> 80 km above the recovered eastward jet in the polar mesosphere (Fig. 16b). These wave forcings were comparable in strength and had values of $-20$ to $-50$ m s$^{-1}$ d$^{-1}$ in the polar MLT. The ES was formed at $z$= ~80 km during 10–13 January. The three-dimensional PW flux suggests that PWs from the lower atmosphere cannot propagate upward through the prevailing westward wind in the stratosphere. Thus, the PWF is likely from PWs generated at > 60° N, $z$= 35–80 km during 10–13 January. These results indicate that both GWF and PWF played significant roles in the formation of the ES. Observed longitudinal structure of the polar temperature suggests that the zonally asymmetric ES was a

warming inside of the polar vortex. The structure of the ES was likely to be determined by the zonally asymmetric GWF (Fig. 16c).

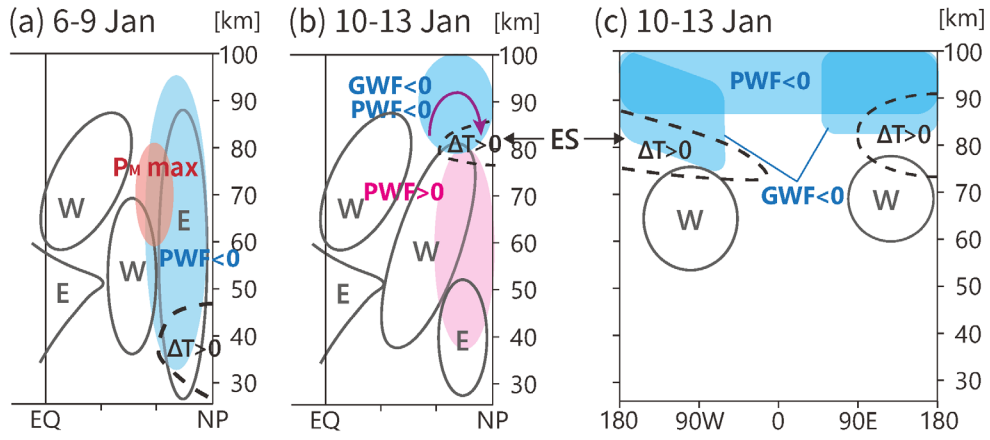


**Figure 16**. A schematic of the formation mechanism of the ES (a, b) in the latitude–height sections and (c) in the longitude-height section. Symbols are the same as those in Fig. 15. Note that the zonal winds, PWF and GWF are for 50° N–70° N and $\Delta T$ is for 70°N–80° N in Fig. 16c.

Our results also suggest that the MIL structure may have affected the process of ES formation. The reformation of the mesospheric westward wind during 6–9 January prevented upward PW propagation. Without adiabatic heating associated with wave forcing, the latitudinal gradient of zonal mean temperature $[T]_y$ tends to decline gradually because of radiative relaxation in the polar night region. The height dependency of $[T]_y$ may be affected by the temperature structure associated with the MIL. The MIL structure had a $[T]$ minimum at $z$= 65–77 km and a maximum at $z$= 80–90 km. At the altitudes where the $[T]$ minimum was present, $[T]_y$ became strongly negative. The altitude of the recovered eastward jet was determined by $[T]_y$ via the thermal wind balance. Thus, the height of the eastward jet was probably modified by the MIL. The eastward jet affected the propagation of GWs and PWs and their forcings in the polar MLT, leading to the formation of the ES. In this way, it is likely that the height of the ES was affected by the MIL.

From the relationship between phase velocity spectra of GW momentum fluxes and the vertical profile of zonal-mean zonal wind, it is shown that vertical propagation from the lower atmosphere alone is insufficient to explain the presence of the GWs, which play important roles in the formation of the MIL and ES. It is suggested that a part of these GWs propagated laterally

and/or were generated in the middle atmosphere. This result indicates that the assumptions generally underlying GW parameterizations are not necessarily appropriate for representing GWs in the MLT.

Results from the high-resolution JAGUAR are generally consistent with observations and enable quantitative analysis of the middle atmosphere dynamics including GWs. Although this study focused on the dynamics in the Northern Hemisphere, JAGUAR provides promising data that can be used to examine the mechanisms of various dynamical phenomena observed in the entire middle atmosphere, such as interhemispheric coupling (e.g., Körnich & Becker, 2010).

## Acknowledgments

All figures in this paper were created using Dennou Club Library (DCL). This study benefitted from stimulating discussions at the International Space Science Institute (ISSI) Gravity Wave activity. The author (HO) is grateful to T. Kinoshita, M. Kohma and S. Noguchi for fruitful discussions. The study was supported by JST CREST (grant JPMJCR1663) and JSPS KAKENHI (grant JP21J20798). The hindcasts were performed using the Earth Simulator at the Japan Agency for Marine-Earth Science and Technology (JAMSTEC). The processed model data are available at the following website: https://pansy.eps.s.u-tokyo.ac.jp/en/archive_data/Okui_etal_2021/. The Aura MLS observation data can be obtained from the NASA Goddard Space Flight Center Earth Science Data and Information Services Center (GES-DISC, https://disc.gsfc.nasa.gov/). The SABER observation data are available from http://saber.gats-inc.com/data.php. This manuscript was grammatically edited by T. Tin from Edanz Group (https://en-author-services.edanz.com/ac).

## References

Andrews, D. G., Holton, J. R., & Leovy, C. B. (1987). *Middle Atmosphere Dynamics*. *International Geophysics Series* (Vol. 40). San Diego, CA: Academic Press.

Andrews, D. G., & McIntyre, M. E. (1976). Planetary Waves in Horizontal and Vertical Shear: The Generalized Eliassen-Palm Relation and the Mean Zonal Acceleration. *Journal of the Atmospheric Sciences*, **33**, 2031–2048. https://doi.org/10.1175/1520-0469(1976)033<2031:PWIHAV>2.0.CO;2

Baldwin, M., & Holton, J. (1988). Climatology of the stratospheric polar vortex and planetary wave breaking. *Journal of the Atmospheric Sciences*, **45**, 1123–1142. https://doi.org/10.1175/1520-0469(1988)045,1123:COTSPV.2.0.CO;2

Bloom, S. C., Takacs, L. L., DaSilva, A. M., & Levina, D. (1996). Data assimilation using incremental analysis updates. *Monthly Weather Review*, **124**, 1256–1271.

780 https://www.researchgate.net/deref/http%3A%2F%2Fdx.doi.org%2F10.1175%2F1520-
781 0493(1996)124%3C1256%3ADAUIAU%3E2.0.CO%3B2

782 Chandran, A., Collins, R. L., Garcia, R. R., & Marsh, D. R. (2011). A case study of an elevated
783 stratopause generated in the Whole Atmosphere Community Climate Model. *Geophysical*
784 *Research Letters*, **38**, L08804. https://doi.org/10.1029/2010GL046566

785 Chandran, A., Collins, R. L., Garcia, R. R., Marsh, D. R., Harvey, V. L., Yue, J., & De La
786 Torre, L. (2013). A climatology of elevated stratopause events in the whole atmosphere
787 community climate model. *Journal of Geophysical Research: Atmospheres*, **118**, 1234–
788 1246. https://doi.org/10.1002/jgrd.50123

789 Chandran, A., Collins, R. L., & Harvey, V. L. (2014). Stratosphere-mesosphere coupling
790 during stratospheric sudden warming events. *Advances in Space Research*, **53**, 1265–1289.
791 https://doi.org/10.1016/j.asr.2014.02.005

792 Charlton, A. J., & Polvani, L. M. (2007). A New Look at Stratospheric Sudden Warmings. Part
793 I: Climatology and Modeling Benchmarks. *Journal of Climate*, **20**, 449–469.
794 https://doi.org/10.1175/JCLI3996.1

795 Charney, J. G., & Drazin, P. G. (1961). Propagation of planetary‐scale disturbances from the
796 lower into the upper atmosphere. *Journal of Geophysical Research*, **66**(1), 83−109.
797 https://doi.org/10.1029/jz066i001p00083

798 Ern, M., Trinh, Q. T., Preusse, P., Gille, J. C., Mlynczak, M. G., Iii, J. M. R., & Riese, M.
799 (2018). GRACILE: A comprehensive climatology of atmospheric gravity wave
800 parameters based on satellite limb soundings. *Earth System Science Data*, **10**, 857–892.
801 https://doi.org/10.5194/essd−10-857-2018

802 France, J. A., & Harvey, V. L. (2013). A climatology of the stratopause in WACCM and the
803 zonally asymmetric elevated stratopause. *Journal of Geophysical Research: Atmospheres*,
804 **118**, 2241–2254. https://doi.org/10.1002/jgrd.50218

805 France, J. A., Harvey, V. L., Randall, C. E., Collins, R. L., Smith, A. K., Peck, E. D., & Fang,
806 X. (2015). A climatology of planetary wave-driven mesospheric inversion layers in the
807 extratropical winter. *Journal of Geophysical Research: Atmospheres*, **120**, 399–413.
808 https://doi.org/10.1002/2014JD022244

809 Funke, B., Ball, W., Bender, S., Gardini, A., Harvey, V. L., Lambert, et al. (2017). HEPPA-II
810 model-measurement intercomparison project: EPP indirect effects during the dynamically
811 perturbed NH winter 2008-2009. *Atmospheric Chemistry and Physics*, **17**, 3573–3604.
812 https://doi.org/10.5194/acp−17-3573-2017

813 Greer, K., Thayer, J. P., & Harvey, V. L. (2013). A climatology of polar winter stratopause
814 warmings and associated planetary wave breaking. *Journal of Geophysical Research:*
815 *Atmospheres*, **118**, 4168–4180. https://doi.org/10.1002/jgrd.50289

816 Harada, Y., Sato, K., Kinoshita, T., Yasui, R., Hirooka, T., & Naoe, H. (2019). Diagnostics of
817 a WN2-Type Major Sudden Stratospheric Warming Event in February 2018 Using a New
818 Three-Dimensional Wave Activity Flux. *Journal of Geophysical Research: Atmospheres*,
819 **124**, 6120–6142. https://doi.org/10.1029/2018JD030162

Harvey, V. L., Randall, C. E., & Hitchman, M. H. (2009). Breakdown of potential vorticity–based equivalent latitude as a vortex-centered coordinate in the polar winter mesosphere. *Journal of Geophysical Research*, **114**, D22105. https://doi.org/10.1029/2009JD012681

Haynes, P. H., McIntyre, M. E., Shepherd, T. G., Marks, C. J., & Shine, K. P. (1991). On the "Downward Control" of Extratropical Diabatic Circulations by Eddy-Induced Mean Zonal Forces. *Journal of Atmospheric Sciences*, **48**(4), 651-678. https://doi.org/10.1175/1520-0469(1991)048%3C0651:OTCOED%3E2.0.CO;2

Hitchman, M. H., & Huesmann, A. S. (2007). A Seasonal Climatology of Rossby Wave Breaking in the 320–2000-K Layer. *Journal of the Atmospheric Sciences*, **64**, 1922–1940. https://doi.org/10.1175/JAS3927.1

Holt, L. A., Randall, C. E., Peck, E. D., Marsh, D. R., Smith, A. K., & Harvey, V. L. (2013). The influence of major sudden stratospheric warming and elevated stratopause events on the effects of energetic particle precipitation in WACCM. *Journal of Geophysical Research: Atmospheres*, **118**, 11,636−11,646. https://doi.org/10.1002/2013JD020294

Kinoshita, T., & Sato, K. (2013). A formulation of unified three-dimensional wave activity flux of inertia-gravity waves and Rossby waves. *Journal of the Atmospheric Sciences*, **70**, 1603–1615. https://doi.org/10.1175/JAS-D−12-0138.1

Kinoshita, T., Sato, K., Ishijima, K., Takigawa, M., & Yamashita, Y. (2019). Formulation of three-dimensional quasi-residual mean flow balanced with diabatic heating rate and potential vorticity flux. *Journal of the Atmospheric Sciences.*, **76**, 851–863. https://doi.org/10.1175/JAS-D−18-0085.1

Körnich, H., & Becker, E. (2010). A simple model for the interhemispheric coupling of the middle atmosphere circulation. *Advances in Space Research*, **45**, 661–668. https://doi.org/10.1016/j.asr.2009.11.001

Koshin, D., Sato, K., Miyazaki, K., & Watanabe, S. (2020). An ensemble Kalman filter data assimilation system for the whole neutral atmosphere. *Geoscientific Model Development*, **13**, 3145–3177. https://doi.org/10.5194/gmd−13-3145-2020

Koshin, D., Sato, K., Kohma, M., & Watanabe, S. (2021). An update on the 4D-LETKF data assimilation system for the whole neutral atmosphere, Geoscientific Model Development Discussion [preprint]. https://doi.org/10.5194/gmd-2020-381, in review.

Labitzke, K. (1981). Stratospheric-mesospheric midwinter disturbances: A summary of observed characteristics, *Journal of Geophysical Research*, **86**(C10), 9665– 9678. https://doi.org/10.1029/JC086iC10p09665

Lait, L. R. (1994). An alternative form for potential vorticity. *Journal of the Atmospheric Sciences*, **51**, 1754–1759. https://doi.org/10.1175/1520-0469(1994)051<1754:AAFFPV>2.0.CO;2

Lieberman, R. S., Riggin, D. M., & Siskind, D. E. (2013). Stationary waves in the wintertime mesosphere: Evidence for gravity wave filtering by stratospheric planetary waves. *Journal of Geophysical Research: Atmospheres*, **118**, 3139– 3149. https://doi.org/10.1002/jgrd.50319

Limpasuvan, V., Orsolini, Y. J., Chandran, A., Garcia, R. R., & Smith, A. K. (2016). On the composite response of the MLT to major sudden stratospheric warming events with

862 elevated stratopause. *Journal of Geophysical Research: Atmospheres*, **121**,4518–4537.
863 https://doi.org/10.1002/2015JD024401

864 Limpasuvan, V., Richter, J. H., Orsolini, Y. J., Stordal, F., & Kvissel, O. K. (2012). The roles
865 of planetary and gravity waves during a major stratospheric sudden warming as
866 characterized in WACCM. *Journal of Atmospheric and Solar-Terrestrial Physics*, **78–79**,
867 84–98. https://doi.org/10.1016/j.jastp.2011.03.004

868 Manney, G. L., Krüger, K., Pawson, S., Minschwaner, K., Schwartz, M. J., Daffer, W. H., et
869 al. (2008). The evolution of the stratopause during the 2006 major warming: Satellite data
870 and assimilated meteorological analyses. *Journal of Geophysical Research*, **113**, D11115.
871 https://doi.org/10.1029/2007jd009097

872 Manney, G. L., Schwartz, M. J., Krüger, K., Santee, M. L., Pawson, S., Lee, J. N., Daffer, W.
873 H., Fuller, R. A., & Livesey, N. J. (2009). Aura Microwave Limb Sounder observations
874 of dynamics and transport during the record-breaking 2009 Arctic stratospheric major
875 warming. *Geophysical Research Letters*, **36**, L12815.
876 https://doi.org/10.1029/2009GL038586

877 Matsuno, T. (1971). A Dynamical Model of the Stratospheric Sudden Warming. *Journal of the*
878 *Atmospheric Sciences.*, **28**, 1479–1494. https://doi.org/10.1175/1520-
879 0469(1971)028<1479:ADMOTS>2.0.CO;2

880 Meraner, K., Schmidt, H., Manzini, E., Funke, B., & Gardini, A. (2016). Sensitivity of
881 simulated mesospheric transport of nitrogen oxides to parameterized gravity waves.
882 *Journal of Geophysical Research: Atmospheres*, **121**, 12,045–12,061.
883 https://doi.org/10.1002/2016JD025012

884 Meriwether, J. W., & Gardner, C. S. (2000). A review of the mesosphere inversion layer
885 phenomenon. *Journal of Geophysical Research*, **105**(D10), 12405– 12416.
886 https://doi.org/10.1029/2000JD900163

887 Meriwether, J. W., & Gerrard, A. J. (2004). Mesosphere inversion layers and stratosphere
888 temperature enhancements. *Reviews of Geophysics*, **42**, RG3003.
889 https://doi.org/10.1029/2003RG000133

890 Orsolini, Y. J., Limpasuvan, V., Pérot, K., Espy, P., Hibbins, R., Lossow, S., et al. (2017).
891 Modelling the descent of nitric oxide during the elevated stratopause event of January
892 2013. *Journal of Atmospheric and Solar-Terrestrial Physics*, **155**, 50–61.
893 https://doi.org/10.1016/j.jastp.2017.01.006

894 Randall, C. E., Harvey, V. L., Holt, L. A., Marsh, D. R., Kinnison, D., Funke, B., & Bernath,
895 P. F. (2015). Simulation of energetic particle precipitation effects during the 2003–2004
896 Arctic winter. *Journal of Geophysical Research: Space Physics*, **120**, 5035–5048.
897 https://doi.org/10.1002/2015JA021196

898 Randall, C. E., Harvey, V. L., Siskind, D. E., France, J., Bernath, P. F., Boone, C. D., & Walker,
899 K. A. (2009). NOx descent in the arctic middle atmosphere in early 2009. *Geophysical*
900 *Research Letters*, **36**, 2007–2010. https://doi.org/10.1029/2009GL039706

901 Rao, J., Garfinkel, C. I., Chen, H., & White, I. P. (2019). The 2019 New Year stratospheric
902 sudden warming and its real-time predictions in multiple S2S models. *Journal of*

903 *Geophysical Research: Atmospheres*, **124**, 11,155–11,174.
904 https://doi.org/10.1029/2019JD030826

905 Sato, K. (1994). A statistical study of the structure, saturation and sources of inertio-gravity
906 waves in the lower stratosphere observed with the MU radar. *Journal of Atmospheric and*
907 *Terrestrial Physics*, **56**(6), 755-774. https://doi.org/10.1016/0021-9169(94)90131-7

908 Sato, K., Kinoshita, T., & Okamoto, K. (2013). A New Method to Estimate Three-Dimensional
909 Residual-Mean Circulation in the Middle Atmosphere and Its Application to Gravity
910 Wave–Resolving General Circulation Model Data. *Journal of the Atmospheric Sciences*,
911 **70**(12), 3756–3779. https://doi.org/10.1175/JAS-D-12-0352.1

912 Sato, K., Kohma, M., Tsutsumi, M., & Sato, T. (2017). Frequency spectra and vertical profiles
913 of wind fluctuations in the summer Antarctic mesosphere revealed by MST radar
914 observations, *Journal of Geophysical Research: Atmospheres*, **122**, 3-19.
915 https://doi.org/10.1002/2016JD025834

916 Sato, K., & Nomoto, M. (2015). Gravity wave-induced anomalous potential vorticity gradient
917 generating planetary waves in the winter mesosphere. *Journal of the Atmospheric*
918 *Sciences*, **72**, 3609–3624. https://doi.org/10.1175/JAS-D−15-0046.1

919 Sato, K., Tateno, S., Watanabe, S., & Kawatani, Y. (2012). Gravity Wave Characteristics in
920 the Southern Hemisphere Revealed by a High-Resolution Middle-Atmosphere General
921 Circulation Model. *Journal of the Atmospheric Sciences*, **69**, 1378–1396.
922 https://doi.org/10.1175/JAS-D−11-0101.1

923 Sato, K., Watanabe, S., Kawatani, Y., Tomikawa, Y., Miyazaki, K., & Takahashi, M. (2009).
924 On the origins of gravity waves in the mesosphere. *Geophysical Research Letters*, **36**,
925 L19801. https://doi.org/10.1029/2009GL039908

926 Sato, K., Yamamori, M., Ogino, S.-Y., Takahashi, N., Tomikawa, Y., & Yamanouchi, T.
927 (2003). A meridional scan of the stratospheric gravity wave field over the ocean in 2001
928 (MeSSO2001). *Journal of Geophysical Research*, **108**, 4491.
929 https://doi.org/10.1029/2002JD003219

930 Sato, K., R. Yasui, & Y. Miyoshi (2018). The momentum budget in the stratosphere,
931 mesosphere, and lower thermosphere. Part I: contributions of different wave types and in
932 situ generation of Rossby waves. *Journal of the Atmospheric Sciences*, **75**, 3613–3633.
933 https://doi.org/10.1175/JAS-D−17-0336.1

934 Salby, M., Sassi, F., Callaghan, P., Wu, D., Keckhut, P., & Hauchecorne, A. (2002).
935 Mesospheric inversions and their relationship to planetary wave structure, *Journal of*
936 *Geophysical Research*, **107**(D4), 4041. https://doi.org/10.1029/2001JD000756

937 Sassi, F., Garcia, R. R., Boville, B. A., & Liu, H. (2002). On temperature inversions and the
938 mesospheric surf zone, *Journal of Geophysical Research*, **107**(D19), 4380.
939 https://doi.org/10.1029/2001JD001525

940 Shibuya, R., & Sato, K. (2019). A study of the dynamical characteristics of inertia-gravity
941 waves in the Antarctic mesosphere combining the PANSY radar and a non-hydrostatic
942 general circulation model. *Atmospheric Chemistry and Physics*, **19**, 3395–3415.
943 https://doi.org/10.5194/acp−19-3395-2019

Shibuya, R., Sato, K., Tsutsumi, M., Sato, T., Tomikawa, Y., Nishimura, K., & Kohma, M. (2017). Quasi−12 h inertia-gravity waves in the lower mesosphere observed by the PANSY radar at Syowa Station (39.6° E, 69.0° S). *Atmospheric Chemistry and Physics*, **17**, 6455–6476. https://doi.org/10.5194/acp−17-6455-2017

Siskind, D. E., Eckermann, S. D., Coy, L., McCormack, J. P., & Randall, C. E. (2007). On recent interannual variability of the Arctic winter mesosphere: Implications for tracer descent. *Geophysical Research Letters*, **34**, L09806. https://doi.org/10.1029/2007GL029293

Siskind, D. E., Eckermann, S. D., McCormack, J. P., Coy, L., Hoppel, K. W., & Baker, N. L. (2010). Case studies of the mesospheric response to recent minor, major, and extended stratospheric warmings. *Journal of Geophysical Research: Atmospheres*, **115**, D00N03. https://doi.org/10.1029/2010JD014114

Siskind, D. E., Sassi, F., Randall, C. E., Harvey, V. L., Hervig, M. E., & Bailey, S. M. (2015). Is a high-altitude meteorological analysis necessary to simulate thermosphere-stratosphere coupling? *Geophysical Research Letters*, **42**, 8225–8230. https://doi.org/10.1002/2015GL065838

Smith, A. K. (1996). Longitudinal Variations in Mesospheric Winds: Evidence for Gravity Wave Filtering by Planetary Waves. *Journal of the Atmospheric Sciences*, **53**, 1156–1173. https://doi.org/10.1175/1520-0469(1996)053<1156:LVIMWE>2.0.CO;2

Smith, A. K. (2003). The Origin of Stationary Planetary Waves in the Upper Mesosphere. *Journal of the Atmospheric Sciences*, **60**, 3033–3041. https://doi.org/10.1175/1520-0469(2003)060<3033:TOOSPW>2.0.CO;2

Smith, A. K., Espy, P. J., López-Puertas, M., & Tweedy, O. V. (2018). Spatial and Temporal Structure of the Tertiary Ozone Maximum in the Polar Winter Mesosphere. *Journal of Geophysical Research: Atmospheres*, **123**, 4373–4389. https://doi.org/10.1029/2017JD028030

Stray, N. H., Orsolini, Y. J., Espy, P. J., Limpasuvan, V., & Hibbins, R. E. (2015). Observations of planetary waves in the mesosphere-lower thermosphere during stratospheric warming events. *Atmospheric Chemistry and Physics*, **15**, 4997–5005. https://doi.org/10.5194/acp−15-4997-2015

Thurairajah, B., Bailey, S. M., Cullens, C. Y., Hervig, M. E., & Russell III, J. M. (2014). Gravity wave activity during recent stratospheric sudden warming events from SOFIE temperature measurements. *Journal of Geophysical Research: Atmospheres*, **119**, 8091–8103. https://doi.org/10.1002/2014JD021763

Thurairajah, B., Cullens, C. Y., Siskind, D. E., Hervig, M. E., & Bailey, S. M. (2020). The role of vertically and obliquely propagating gravity waves in influencing the polar summer mesosphere. *Journal of Geophysical Research: Atmospheres*, **125**, e2020JD032495. https://doi.org/10.1029/2020JD032495

Tomikawa, Y., Sato, K., Watanabe, S., Kawatani, Y., Miyazaki, K., & Takahashi, M. (2012). Growth of planetary waves and the formation of an elevated stratopause after a major stratospheric sudden warming in a T213L256 GCM. *Journal of Geophysical Research: Atmospheres*, **117**, D16101. https://doi.org/10.1029/2011JD017243

Vadas, S. L., & Becker, E. (2018). Numerical modeling of the excitation, propagation, and dissipation of primary and secondary gravity waves during wintertime at McMurdo Station in the Antarctic. *Journal of Geophysical Research: Atmospheres*, **123**, 9326–9369. https://doi.org/10.1029/2017JD027974

Watanabe, S., Kawatani, Y., Tomikawa, Y., Miyazaki, K., Takahashi, M., & Sato, K. (2008). General aspects of a T213L256 middle atmosphere general circulation model. *Journal of Geophysical Research: Atmospheres*, **113**, D12110. https://doi.org/10.1029/2008JD010026

Watanabe, S., & Miyahara, S. (2009). Quantification of the gravity wave forcing of the migrating diurnal tide in a gravity wave-resolving general circulation model. *Journal of Geophysical Research: Atmospheres*, **114**, D07110. https://doi.org/10.1029/2008JD011218

Watanabe, S., Tomikawa, Y., Sato, K., Kawatani, Y., Miyazaki, K., & Takahashi, M. (2009). Simulation of the eastward 4-day wave in the Antarctic winter mesosphere using a gravity wave resolving general circulation model. *Journal of Geophysical Research: Atmospheres*, **114**, D16111. https://doi.org/10.1029/2008JD011636

Yamashita, C., England, S. L., Immel, T. J., & Chang, L. C. (2013). Gravity wave variations during elevated stratopause events using SABER observations. *Journal of Geophysical Research: Atmospheres*, **118**, 5287–5303. https://doi.org/10.1002/jgrd.50474

Yasui, R., K. Sato, & Y. Miyoshi. (2018). The momentum budget in the stratosphere, mesosphere, and lower thermosphere. Part II: The in situ generation of gravity waves. *Journal of the Atmospheric Sciences*, **75**, 3635–3651. https://doi.org/10.1175/JAS-D−17-0337.1